# 9

# Hyperspectral Remote Sensing for Terrestrial Applications

Prasad S. Thenkabail
*U. S. Geological Survey*

Pardhasaradhi Teluguntla
*U. S. Geological Survey*
*and*
*Bay Area Environmental Research Institute*

Murali Krishna Gumma
*International Crops Research Institute for the Semi Arid Tropics*

Venkateswarlu Dheeravath
*United Nations World Food Programme*



## Acronyms and Definitions

| | |
|---|---|
| ASD | Analytical spectral devices |
| AISA | Airborne imaging spectrometer for applications |
| AVIRIS | Airborne visible/infrared imaging spectrometer sensor |
| CHRIS PROBA | Compact High Resolution Imaging Spectrometer Project for On-Board Autonomy, Belgian Satellite |
| DHVIs | Derivative hyperspectral vegetation indices (DHVIs) |
| DNs | Digital numbers |
| EnMAP | Environmental Mapping and Analysis Program, Genrman's hyperspectral satellite mission |
| EO-1 | Earth Observing-1 satellite of NASA |
| GnyLi | A hyperspectral vegetation index involving 5 hyperspectral narrow bands developed by Martin Gnyp Leon, Fei Li, and Georg Bareth et al. |
| HICO | Hyperspectral Imager for Coastal Oceans sensor, NASA's Hyperspectral Imager for the Coastal Ocean (HREP-HICO) |
| HBSIs | Hyperspectral biomass and structural indices |
| HNBs | Hyperspectral narrow bands |
| HVIs | Hyperspectral vegetation indices (HVIs) |
| HyspIRI | Hyperspectral infrared imager, next-generation hyperspectral sensor by NASA |
| MBHVI | Multiple band hyperspectral vegetation indices |
| MNF | Minimum noise fraction |
| NASA | National Atmospheric and Space Administration |

| | |
|---|---|
| OHNBs | Optimum hyperspectral narrow bands |
| OMI | *Ozone Monitoring Instrument onboard Aura satellite* |
| PCA | Principal component analysis |
| PRISMA | *Hyperspectral* Precursor and Application Mission or PRecursore IperSpettrale della Missione Applicativa of Italy |
| SCIAMACHY | Scanning Imaging Absorption spectroMeter for Atmospheric CartograpHY, hyperspectral sensor onboard European Space Agencies (ESA's) ENVISAT |
| SMA | Spectral mixture analysis |
| SMT | Spectral matching techniques |
| SVM | Support vector machines |
| TBHVIs | Two-band hyperspectral vegetation indices |
| VNIR | Visible and nearinfrared (VNIR) |
| WSA | Whole spectral analysis |

## 9.1 Introduction

Remote sensing data are considered hyperspectral when the data are gathered from numerous wavebands, contiguously over an entire range of the spectrum (e.g., 400–2500 nm). Goetz (1992) defines hyperspectral remote sensing as "The acquisition of images in hundreds of registered, contiguous spectral bands such that for each picture element of an image it is possible to derive a complete reflectance spectrum." However, Jensen (2004) defines hyperspectral remote sensing as "The simultaneous acquisition of images in many relatively narrow, contiguous and/or non contiguous spectral bands throughout the ultraviolet, visible, and infrared portions of the electromagnetic spectrum."

Overall, the three key factors in considering data to be hyperspectral are the following:

1. *Contiguity in data collection*: Data are collected contiguously over a spectral range (e.g., wavebands spread across 400–2500 nm).
2. *Number of wavebands*: The number of wavebands by itself does not make the data hyperspectral. For example, if there are numerous narrowbands in 400–700 nm wavelengths, but have only a few broadbands in 701–2500 nm, the data cannot be considered hyperspectral. However, even relatively broad bands of width, say, for example, 30 nm bandwidths spread equally across 400–2500 nm, for a total of ~70 bands, are considered hyperspectral due to contiguity.
3. *Bandwidths*: Often, hyperspectral data are collected in very narrow bandwidths of ~1 to ~10 nm, contiguously over the entire spectral range (e.g., 400–2500 nm). Such narrow bandwidths are required to get hyperspectral signatures. But one can have a combination of narrowbands and broadbands spread across the spectrum and meet the criterion for hyperspectral remote sensing.

In summary

Remote sensing data are called hyperspectral when the data are collected contiguously over a spectral range, preferably in narrow bandwidths and in reasonably high number of bands.

Such a definition will meet many requirements and expectations of hyperspectral data.

Hyperspectral remote sensing is also referred to as imaging spectroscopy since data for each pixel are acquired in numerous contiguous wavebands resulting in (1) 3d image cube and (2) hyperspectral signatures. The various forms and characteristics of hyperspectral data (imaging spectroscopy) are illustrated in Figures 9.1 through 9.7. The distinction between hyperspectral and multispectral is based on the narrowness and contiguous nature of the measurements, not the "number of bands" (Qi et al., 2012).

The overarching goal of this chapter is to provide an introduction to hyperspectral remote sensing, its characteristics, data mining approaches, and methods of analysis for terrestrial application. First, hyperspectral sensors from various platforms are

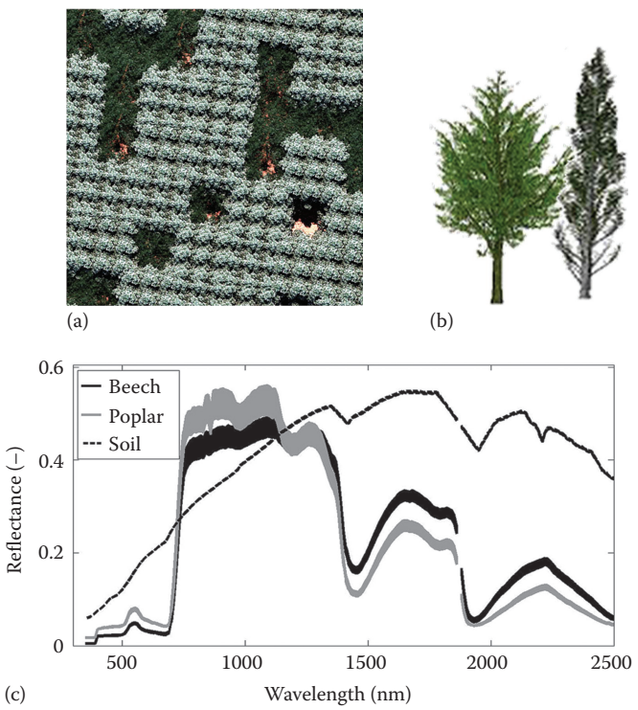


**FIGURE 9.1** Tree spectra. Analytical Spectral Devices (ASD) FieldSpec JR spectroradiometer. Hyperspectral shape-based unmixing to improve intra- and interclass variabilities for forest and agro-ecosystem monitoring. A detail of a 30-by-30 m image pixel of the virtual forest consisting of two species with a different structure, with 10% of the trees removed to include gaps in the canopy (a). An example of a virtual tree for the two species, used to build up the forest, is shown in (b), while the spectral variability of the two species and the soil is given as well (c). (From Tits, L. et al., *ISPRS J. Photogramm. Remote Sens.*, 74, 163, 2012.)

noted. Second, data mining to overcome data redundancy is enumerated. Third, concept of Hughes's phenomenon and the need to overcome it are highlighted. Fourth, hyperspectral data analysis methods are presented and discussed. Methods section includes approaches to optimal band selection, deriving hyperspectral vegetation indices (HVIs) and various classification methods.

## 9.2 Hyperspectral Sensors

Hyperspectral data (or imaging spectroscopy) are gathered from various sensors. These are briefly discussed in the following text.

### 9.2.1 Spectroradiometers

The most common and widely used over last 50 years is hand-held or platform-mounted spectroradiometers. Typically, spectroradiometers gather hyperspectral data ~1 nm wide narrowbands over the entire spectral range (e.g., 400–13,500 nm). For example, Figure 9.1 illustrates the hyperspectral data gathered for Beech versus Poplar forests (Thomas, 2012; Tits et al., 2012; Zhang, 2012; Tanner, 2013) based on FieldSpec Pro FR spectroradiometer manufactured by Analytical Spectral Devices (ASD). Data are acquired over 400–2,500 nm at every 1 nm bandwidth. Gathering spectra at any given location involved optimizing the integration time (typically set at 17 ms), providing foreoptic information, recording dark current, collecting white reference reflectance, and then obtaining target reflectance at set field of view such as 18° (Thenkabail et al., 2004a). Data are either in radiance (W $m^{-2}$ $sr^{-1}$ $\mu m^{-1}$) or reflectance factor as shown in Figure 9.1 or in percentage.

### 9.2.2 Airborne Hyperspectral Remote Sensing

Airborne hyperspectral remote sensing platform is the next most common hyperspectral data, which has a history of over 30 years. The most common is the airborne visible/infrared imaging spectrometer (AVIRIS) by NASA's Jet Propulsion Laboratory (JPL). As an imaging spectrometer, AVIRIS gathers data in 614-pixel swath, in 224 bands, over 400–2500 nm wavelength. The data can be constituted as image cube (e.g., Figure 9.2; [Guo et al., 2013]). Figure 9.2 shows hyperspectral imaging data gathered by AVIRIS over an agricultural area. The hyperspectral signatures of tilled versus untilled lands of corn and soybean farms as well as few other crops are illustrated by Guo et al. 2013 (Figure 9.2). Spectral reflectivity of no-till corn fields is highest in the red (around 680 nm). In contrast, grass/pasture and woods are highest around 680 nm, and reflectivity is highest for these land covers in the near-infrared (NIR; 760–900 nm). The healthy grass/pasture and woods also absorb heavily around 960–970 nm range. There are many other unique features that can even be observed qualitatively by someone trained in imaging spectroscopy.

Another frequently used airborne hyperspectral imager is the Australian HyMap. It has 126 wavebands over 400–2500 nm. The data captured by HyMap are illustrated in Figure 9.3 (Andrew and Ustin, 2008). Typical characteristics of healthy vegetation for certain species is obvious as described earlier for wavelengths centered in red and NIR. In contrast, the soil and the litter have comparable spectra, with litter having higher reflectivity than soil in NIR and SWIR bands. Water absorbs heavily in NIR and SWIR, and hence the reflectivities are very low or zero (Figure 9.3).

### 9.2.3 Spaceborne Hyperspectral Data

In the year 2000, NASA launched the first civilian spaceborne hyperspectral imager called Hyperion onboard Earth Observing-1 (EO-1) satellite. Hyperion gathers data in 242 bands spread across 400–2500 nm. Each band is 10 nm wide. Of the original 242 Hyperion bands, 196 are unique and calibrated: bands 8 (427.55 nm) to 57 (925.85 nm) from the visible and near-infrared (VNIR) sensors, and bands 79 (932.72 nm) to 224

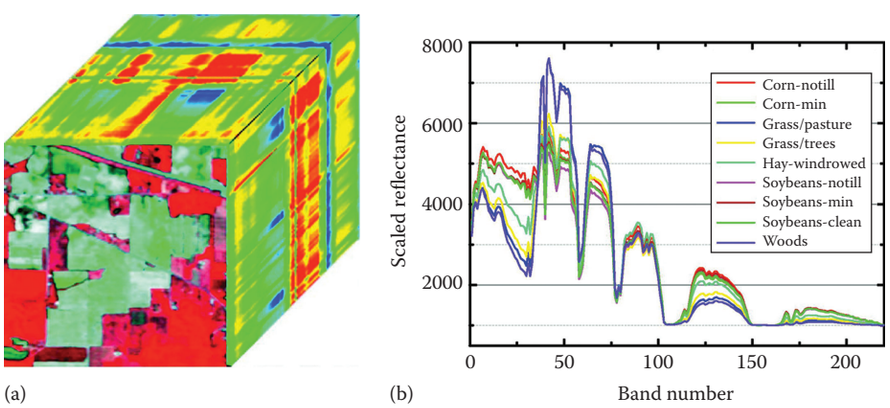


**FIGURE 9.2** Corn-till. AVIRIS Indian Pines data set: (a) 3D hyperspectral cube and (b) the scaled reflectance plot. (From Guo, X. et al., *ISPRS J. Photogramm. Remote Sens.*, 83, 50, 2013.)

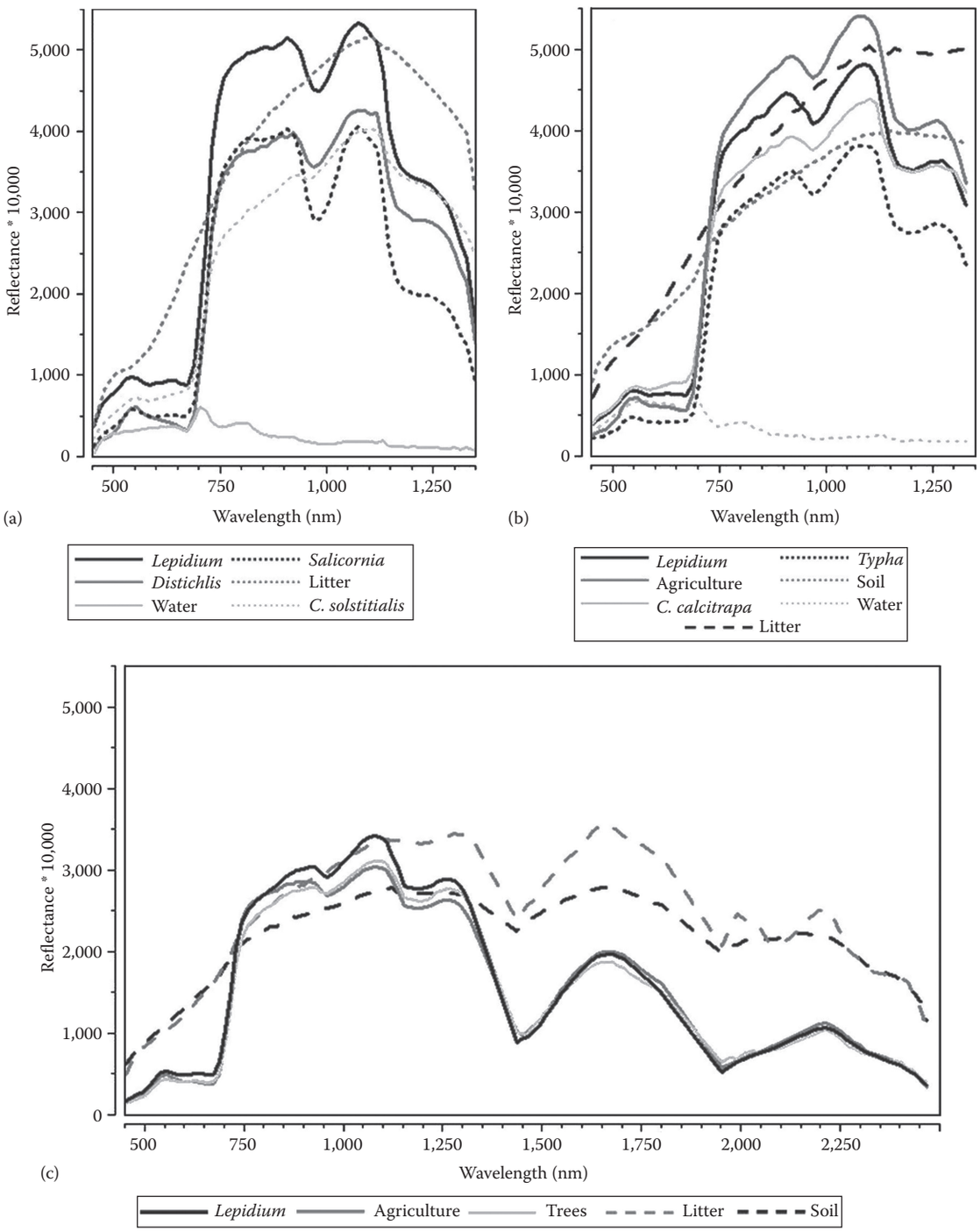


**FIGURE 9.3** Reflectance spectra derived from HyMap imagery of the dominant species at (a) Rush Ranch, (b) Jepson Prairie, and (c) Consumes River Preserve. These spectra were used as training end members for the mixture-tuned matched filtering (MTMF). (From Andrew, M.E. and Ustin, S.L., *Remote Sens. Environ.,* 112, 4301, 2008.)

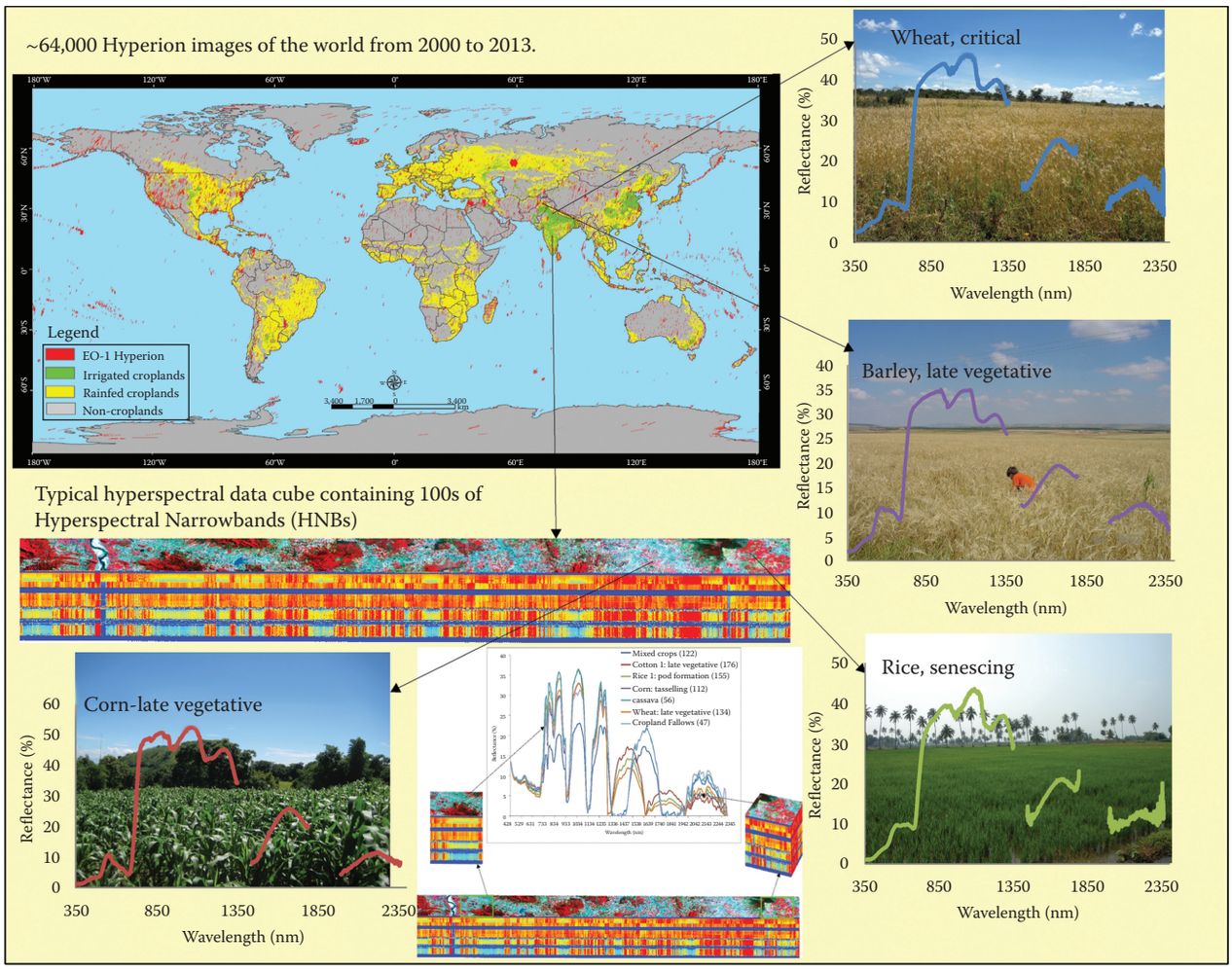


**FIGURE 9.4** EO-1 Hyperion is the first spaceborne civilian hyperspectral sensor that was launched in year 2000 and has so far acquired ~64,000 images of the world (see the area covered by Hyperion images marked in red on global image). Each image is 7.5 km by 185 km, has 242 bands over 400–2500 nm. A single such image data cube is shown in the center with spectral signatures derived from the Hyperion sensor shown for few land cover themes. Typical ASD spectroradiometer gathered hyperspectral data of crops are shown in photos. The gaps in ASD hyperspectral data are in areas of atmospheric windows where data is too noisy and hence deleted. (Plotted using Data available from http://earthexplorer.usgs.gov/; http://eo1.gsfc.nasa.gov/.)

(2395.53 nm) from the SWIR sensors (Thenkabail et al., 2004b). The redundant and uncalibrated bands are in the spectral range: 357–417, 936–1068, and 852–923 nm. The 196 bands are further reduced to 157 bands after dropping bands in atmospheric windows: 1306–1437, 1790–1992, and 2365–2396 nm ranges, which show high noise level (Thenkabail et al., 2004b).

From year 2000 to 2014, Hyperion has acquired ~64,000 images spread across the world (Figure 9.4) that are now freely available from the U.S. Geological Survey's (USGS) EarthExplorer and Glovis portals. Each image is 7.5 km by 185 km with a pixel resolution of 30 m. The data cubes composed from these images allow us to derive hyperspectral signature banks of various land cover or cropland themes (e.g., Figure 9.4). Figure 9.5a illustrates two Hyperion images acquired over California as well as a number of hyperspectral signatures of major crops gathered using ASD field spectroradiometer.

### 9.2.4 Unmanned Aerial Vehicles

Hyperspectral sensors are increasingly carried onboard unmanned aerial vehicles (UAVs; Colomina and Molina, 2014). The UAVs are fast evolving as widely used remote sensing platform. A wide array of UAVs (e.g., Figure 9.5b) are currently used to carry hyperspectral sensors as well as many different types of sensors.

### 9.2.5 Multispectral versus Hyperspectral

Whereas multispectral broadband data-acquired from sensors such as the Landsat ETM+ only offer few possibilities, in contrast Hyperion offers many possibilities for visualizations and quantification of terrestrial earth features (e.g., Figure 9.6). In Figure 9.6, depiction of different false color composites (FCCs) of Hyperion (e.g., RGB: 843, 680, 547 nm; or RGB: 680, 547, 486 nm, and so on)

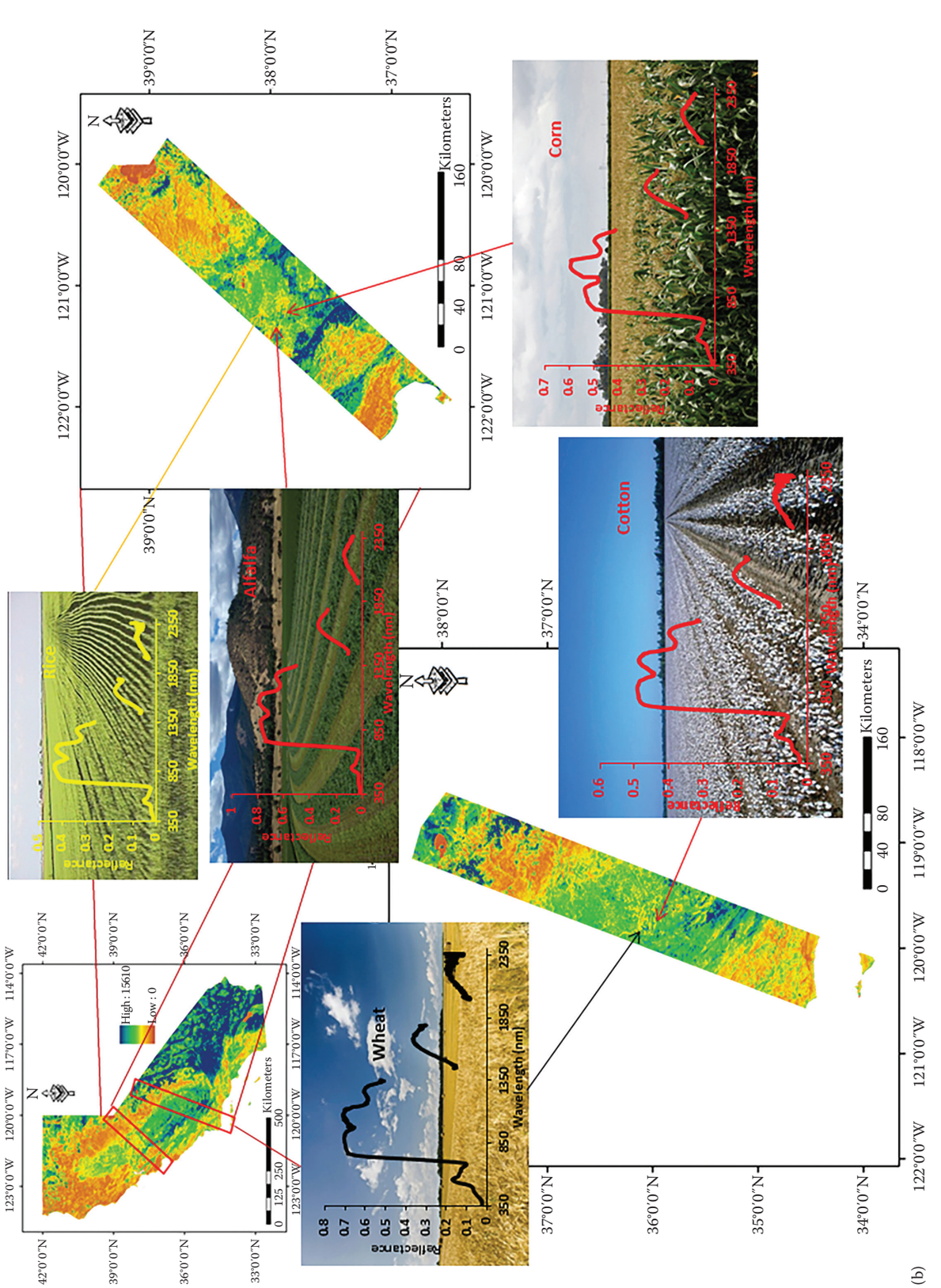


**FIGURE 9.5** Hyperspectral spectral signatures of some of the major crops of California. The depicted spectral signatures are representative of the particular crops measured using ASD spectroradiometer. Two Hyperion images (each of 7.5 km by 185 km) are also illustrated. (a) Microdrone MD4–1000 flying over the experimental crop. (From Torres-Sánchez, J. et al., *Comput. Electron. Agric.*, 103, 104, 2014.) (*Continued*)

(a)

**FIGURE 9.5** (*Continued*) Hyperspectral spectral signatures of some of the major crops of California. The depicted spectral signatures are representative of the particular crops measured using ASD spectroradiometer. Two Hyperion images (each of 7.5 km-by-185 km) are also illustrated. (a) Microdrone MD4–1000 flying over the experimental crop.

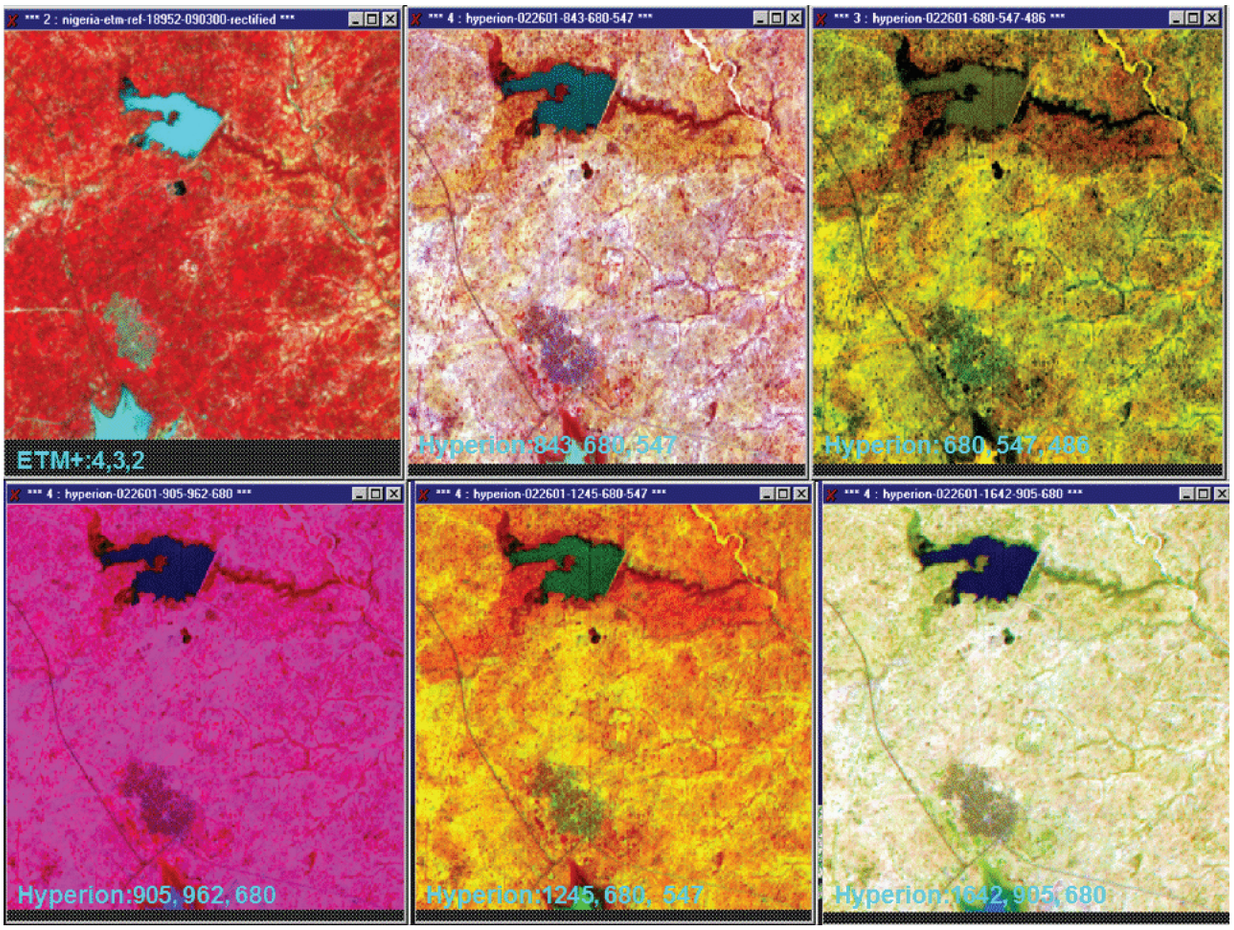


**FIGURE 9.6** Hyperion images displayed in a number of different combinations of false color composites (FCCs) (e.g., wavebands centered at 843, 680, 547 nm, which are NIR, red, green as RGB FCC) and compared with classic RGB 4, 3, 2 (NIR, red, green) FCC combination of Landsat ETM+ data on top left. Unlike multispectral data, hyperspectral data offer numerous different opportunities to depict, quantify, and study the Planet Earth.

and comparison with FCC of Landsat ETM+ bands 4, 3, 2 clearly demonstrate, even by visual observation, the many possibilities that exist with Hyperion. For example, a seven-band Landsat will provide 21 unique indices ($7 \times 7 = 49$ indices – 7 indices on the diagonal of the matrix divided by 2 since the values above and below the matrix are transpose of each other). In contrast, 157-band clean Hyperion data (after reduced from original 242 bands by eliminating bands in atmospheric windows and uncalibrated bands) allow for 12,246 unique indices ($157 \times 157 = 24{,}640$ indices—157 indices on the diagonal of the matrix divided by 2 since the values above and below the matrix are the transpose of each other).

### 9.2.6 Hyperspectral Data: 3D Data Cube Visualization and Spectral Data Characterization

One quick way to visualize the hyperspectral data is to create 3D cubes as illustrated by an EO-1 Hyperion data in Figure 9.7. The 3D cube basically is a data layer stack of 242 bands over 400–2500 nm. Looking through this stack, when there is same color along the bands 1–242, it indicates less diversity in data. The spectral regions with significant diversity are in different color (e.g., red versus cyan in Figure 9.7). Hyperion digital numbers (DNs) are 16-bit radiances and are stored as 16-bit signed integer, which are then converted to radiances using a scaling factor provided in the header file, then to at-sensor reflectance, and finally to ground reflectance (see Thenkabail et al., 2004b). So, a click on any pixel will give reflectances in 242 bands, which is then plotted as hyperspectral signature (e.g., Figure 9.6) and analyzed quantitatively.

### 9.2.7 Past, Present, and Near-Future Spaceborne Hyperspectral Sensors

Hyperspectral sensors are of increasing interest to the remote sensing community given its their natural inherent advantages over multispectral sensors (Qi et al., 2012; Thenkabail et al., 2012a). As a result, we are seeing a number of spaceborne

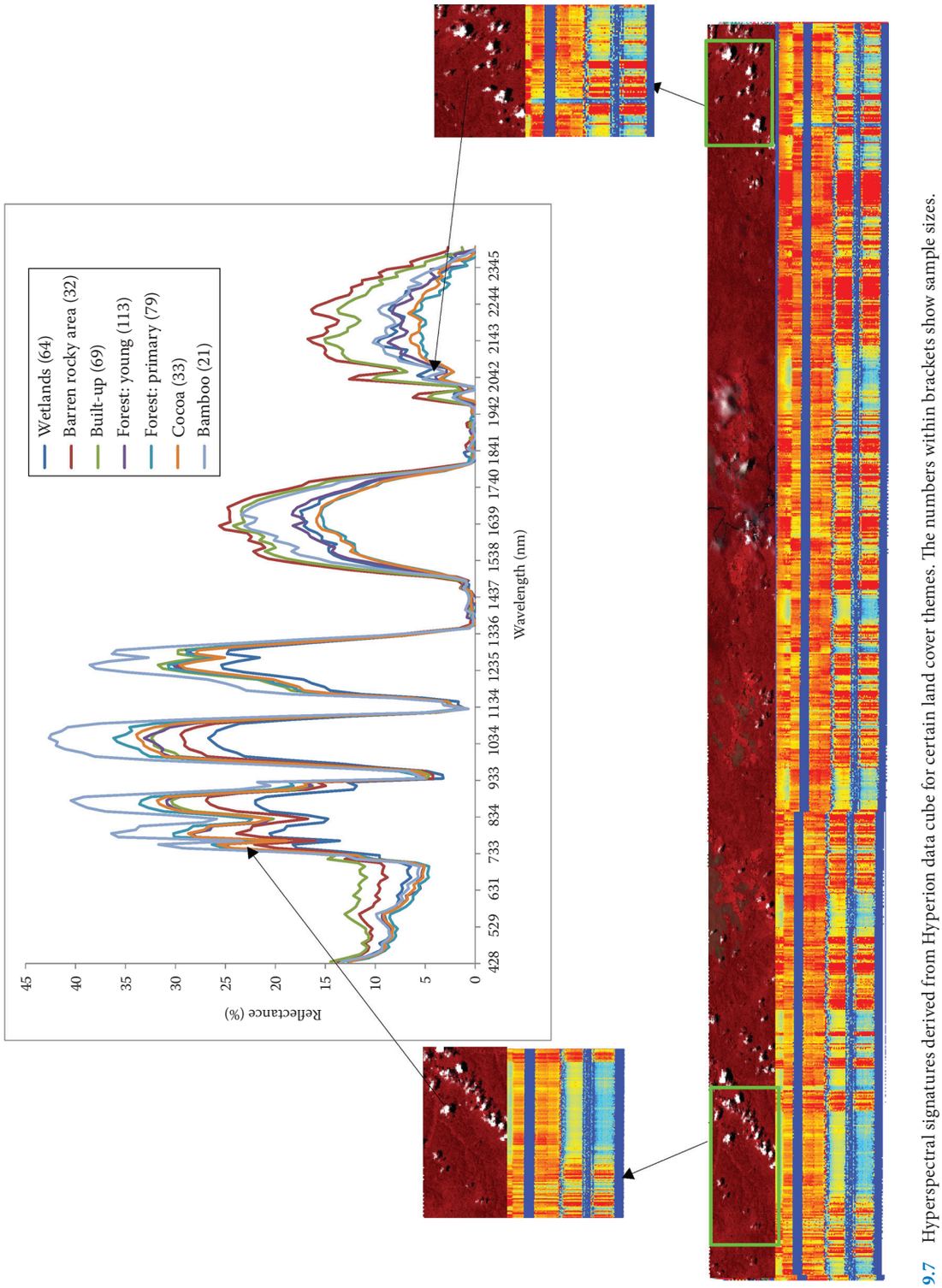


**FIGURE 9.7** Hyperspectral signatures derived from Hyperion data cube for certain land cover themes. The numbers within brackets show sample sizes.

hyperspectral imagers for Ocean, Atmosphere, and Land (Table 9.1). These include (Table 9.1) NASA's Hyperion, HyspIRI, OMI, HICO, German's EnMap, Italy's PRISMA, ESA's SCIAMACHY, and CHRIS PROBA (Miura and Yoshioka, 2012; Ortenberg, 2012; Qi et al., 2012). There are also current initiatives from private industry in the commercial sector, like that from Boeing to launch hyperspectral sensors. The spatial, spectral, radiometric, and temporal characteristics of some of the key ocean, atmospheric, and land observation spaceborne hyperspectral data are provided in Table 9.1.

### 9.2.8 Data Normalization Hyperspectral Data

We illustrate the hyperspectral data normalization taking the case of Hyperion data. The DNs of the Hyperion level 1 products are 16-bit radiances and are stored as 16-bit signed integers. The DNs were converted to radiances (W $m^{-2}$ $sr^{-1}$ $\mu m^{-1}$) using an appropriate scaling (e.g., for a Hyperion image dated March 21, 2002, factor: 40 for visible and VNIR, and 80 for SWIR). However, users should check the header file of the image they work with to determine the exact scaling factor for their image.

*Radiance* (W $m^{-2}$ $sr^{-1}$ $\mu m^{-1}$) for VNIR bands = DN/40
*Radiance* (W $m^{-2}$ $sr^{-1}$ $\mu m^{-1}$) for SWIR bands = DN/80
*Radiance to at-sensor top of atmosphere reflectance is then calculated using*

$$\textit{Reflectance (\%)} = \text{n}\frac{\pi L_\lambda d^2}{ESUN_\lambda \cos\theta_S}$$

where, TOA reflectance (at-satellite exoatmospheric reflectance)
$L_\lambda$ is the radiance (W $m^{-2}$ $sr^{-1}$ $\mu m^{-1}$)
d is the earth-to-sun distance in astronomic units at the acquisition date (see Markham and Barker, 1987)
$ESUN_\lambda$ is the irradiance (W $m^{-2}$ $sr^{-1}$ $\mu m^{-1}$) or solar flux (Neckel and Labs, 1984)
$\theta_s$ is the solar Zenith angle

*Note*: $\theta_s$ is solar Zenith angle in degrees (i.e., 90° minus the sun elevation or sun angle when the scene was recorded as given in the image header file).
Atmospheric correction methods include (1) dark object subtraction technique (Chavez, 1988), (2) improved dark object subtraction technique (Chavez, 1989), (3) radiometric normalization technique: Bright and dark object regression (Elvidge et al., 1995), and (4) 6S model (Vermote et al. 2002). Readers with further interest in this topic are referred to Chapters 4 through 8 in *Remotely Sensed Data Characterization, Classification, and Accuracies* and Chander et al. (2009).

## 9.3 Data Mining and Data Redundancy of Hyperspectral Data

Data mining is one of the critical first steps in hyperspectral data analysis. The primary goal of data mining is to eliminate redundant data and retain only the useful data. Data volumes are reduced through data mining methods such as feature selection (e.g., principal component analysis (PCA), derivative analysis, and wavelets), lambda-by-lambda correlation plots (Thenkabail et al., 2000), minimum noise fraction (MNF) (Green et al., 1988; Boardman and Kruse, 1994), and HVIs (e.g., Thenkabail et al., 2014). Data mining methods lead to (Thenkabail et al., 2012b) (1) reduction in data dimensionality, (2) reduction in data redundancy, and (3) extraction of unique information.

It is a well-known fact that wavebands adjacent to one another (e.g., 680 nm versus 690 nm or 550 nm versus 560 nm) are often highly correlated for a given application. In various research papers, Thenkabail et al. (2000, 2004a,b, 2010, 2012b, 2014), Numata (2012), and Thenkabail and Wu (2012) showed that in a large stack of 242 bands in a Hyperion data, typically ~10% of the wavebands (~20 bands) are very useful in agricultural cropland or vegetation studies. It means for any one given application (e.g., agriculture), a large number of bands are likely to be redundant. So, the goal of the data mining is to identify and eliminate redundant bands. This will help eliminate unnecessary processing of redundant data, at the same time retaining the optimal power of hyperspectral data. This process is of great importance at a time when "big data" are the norm of the times.

However, eliminating redundant bands needs to be done with considerable care and expertise. What is redundant for one application (e.g., agriculture; [Yao et al., 2011]) may be critical for another application (e.g., geology).

Data mining requires merging of different disciplines such as digital imagery, pattern recognition, database, artificial intelligence, machine learning, algorithms, and statistics. There are various models of data mining. The generic concept of data mining is illustrated in Figure 9.8 (Lausch et al., 2014). Figure 9.9 (Lausch et al., 2014) shows data mining model applications for studies in soil clay content and soil organic content.

## 9.4 Hughes' Phenomenon and the Need for Data Mining

If the number of bands remains high, the number of observations required to train a classifier increases exponentially to maintain classification accuracies, which is called Hughes's phenomenon (Thenkabail and Wu, 2012). For example, Thenkabail et al. (2004a, b) used 20 Hyperion bands to classify five crop types and achieve an accuracy of 90%. Relative to this, the seven-band Landsat data provided only an accuracy of 60% in classifying the same five crops. However, the number of observation points (e.g., ground data) to train and test the algorithms will be exponentially higher for the Hyperion data relative to Landsat data because larger numbers of bands are involved with Hyperion. So, one needs to weigh the higher classification accuracies achieved using greater number of bands versus the resources required to gather exponentially

**TABLE 9.1** Characteristics of Spaceborne Hyperspectral Sensors (Either in Orbit or Planned for Launch) for Ocean, Atmosphere, Land, and Water Applications Compared with ASD Spectroradiometer[a]

| Sensor, Satellite[c] | Spatial (m) | Spectral (#) | Swath (km) | Band Range (μm) | band Widths (μm) | Irradiance (W m−Wsr−r μm−μ) | Data Points (# per ha) | Launch (Date) |
|---|---|---|---|---|---|---|---|---|
| 1. Coastal hyperspectral spaceborne imagers | | | | | | | | |
| a. HICO, ISS USA | 90 | 128 | 42 | 353–1,080 | 5.7 | See data in Neckel and Labs (1984). Plot it | 0.81 | 2009–present |
| 2. Atmosphere\ozone hyperspectral spaceborne imagers | | | | | | | | |
| a. OMI, Aura USA | 13,000 × 12,000 | 740 | 145 | 270–500 | 0.45–1 | See data in Neckel and Labs (1984). Plot it | 1/16,900 | 2004–present |
| b. SCIAMACHY, ENVISAT ESA | 30,000 × 60,000 | ~2,000 | 960 | 212–2,384 | 0.2–1.5 | See data in Neckel and Labs (1984). Plot it | 1/180,000 | 2002–present |
| 3. Land and water hyperspectral spaceborne imagers | | | | | | | | |
| a. Hyperion, EO-1 USA | 30 | 220 (196[b]) | 7.5 | 196 effective Calibrated bands VNIR (band 8–57) 427.55–925.85 nm SWIR (band 79–224) 932.72–23,95.53 nm | 10 nm wide (approx.) for all 196 bands | See data in Neckel and Labs (1984). Plot it and obtain values for Hyperion bands | 11.1 | 2000–present |
| b. CHRIS, PROBA ESA | 25 | 19 | 17.5 | 200–1,050 | 1.25–11 | Same as above | 16 | 2001–present |
| c. HyspIRI VSWIR USA | 60 | 210 | 145 | 210 bands in 380–2,500 nm | 10 nm wide (approx.) for all 210 bands | See data in Neckel and Labs (1984). Plot it | 2.77 | 2020+ |
| d. HyspIRI TIR USA | 60 | 8 | 145 | 7 bands in 7,500–12,000 nm and 1 band in 3,000–5,000 nm (3,980 nm center) | 7 bands in 7,500–12,000 nm | See data in Neckel and Labs (1984). Plot it | 2.77 | 2020+ |
| e. EnMAP Germany | 30 | 92 | 30 | 420–1,030 | 5–10 | Same as above | 11.1 | 2015+ |
| | | 108 | | 950–2,450 | 10–20 | | | |
| f. PRISMA Italy | 30 | 250 | 30 | 400–2,500 | <10 | Same as above | 11.1 | 2014+ |
| 4. Land and Water Hand-held spectroradiometer | | | | | | | | |
| a. ASD spectroradiometer | 1,134 $cm^2$ @ 1.2 m Nadir view 18° Field of view | 2,100 bands 1 nm width between 400 and 2,500 nm | N/A | 2,100 effective bands | 1 nm wide (approx.) in 400–2,500 nm | See data in Neckel and Labs (1984). Plot it and obtain values for Hyperion bands | 88,183 | Last 30+ years |

*Sources:* Thenkabail, P.S. et al., 2012; Thenkabail, P.S. et al., *Photogramm. Eng. Remote Sens.*, 80, 697, 2014; Qi, J. et al., Hyperspectral sensor systems and data characteristics in global change studies, Chapter 3, in Thenkabail, P.S., Lyon, G.J., and Huete, A. 2012, *Hyperspectral Remote Sensing of Vegetation*, CRC Press/Taylor & Francis Group, Boca Raton, FL, London, FL, New York, 2011, pp. 69–92.

[a] Information for the table modified and adopted from Thenkabail et al., 2011, Thenkabail et al., 2014, and Qi et al., 2014.

[b] Of the 242 bands, 196 are unique and calibrated. These are: (1) Band 8 (427.55 nm) to band 57 (925.85 nm) that are acquired by visible and near-infrared (VNIR) sensor; and (2) Band 79 (932.72 nm) to band 224 (2395.53 nm) that are acquired by short wave infrared (SWIR) sensor

[c] HICO, **Hyperspectral** Imager for the Coastal Ocean onboard International Space Station; OMI, Ozone Monitoring Instrument onboard AURA of NASA; SCIAMACHY, Scanning Imaging Absorption Spectrometer for Atmospheric CHartographY of ESA; Hyperion EO-1, hyperspectral sensor onboard; EO-1, Earth observing 1; CHRIS PROBA, Compact High Resolution Imaging Spectrometer Project for On Board Autonomy satellite of ESA; HyspIRI VSWIR, Hyperspectral Infrared Imager Visible to Short Wavelength InfraRed of NASA; HyspIRI TIR, Hyperspectral Infrared Imager thermal infrared of NASA; Environmental Mapping and Analysis Program of Germany; PRISMA, PRecursore IperSpettrale della Missione Applicativa of Italy.

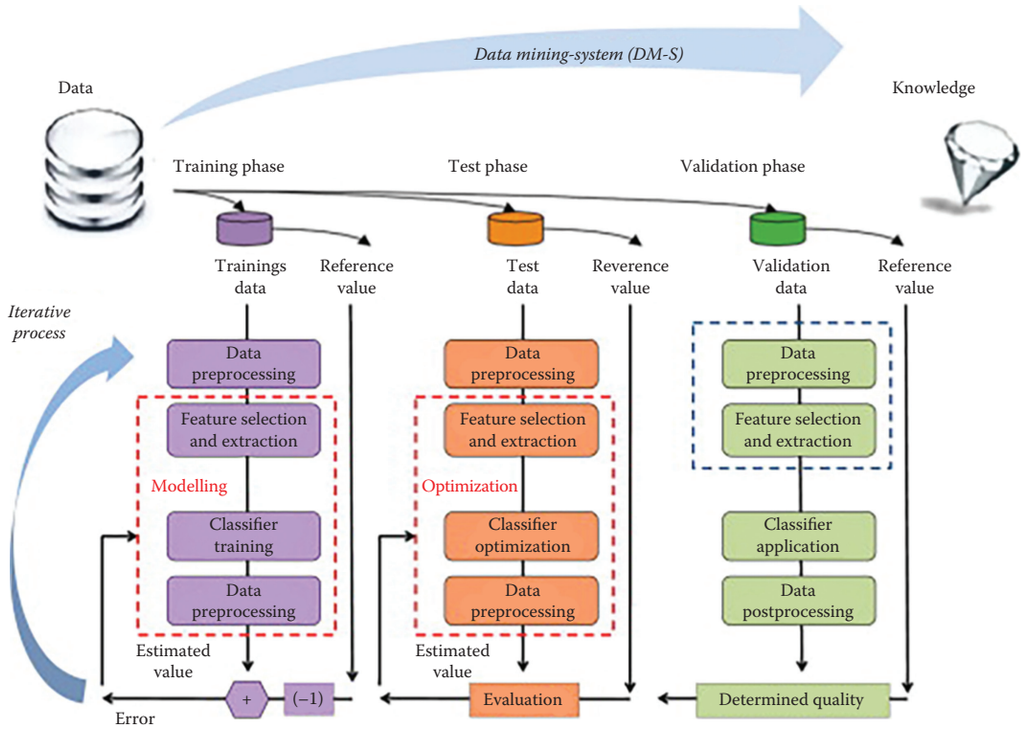


**FIGURE 9.8** Data mining 1. Data mining and linked open data—New perspectives for data analysis in environmental research. Data mining process with the data mining system (DM-S) in the phases: (1) training phase, (2) test phase, and (3) validation phase. The data mining process works in a comparable way in all types of data mining types like text mining or web mining (changed according to Fayyad et al., (1996) and Tanner (2013). (From Lausch, A. et al., *Ecol. Model.*, 2014.)

higher number of observation (e.g., ground data) required to train and test the algorithms. So, higher accuracy by as much as 30% using 20 hyperspectral narrowbands (HNBs) when compared with seven-band Landsat will justify the greater number of ground data required. However, beyond 20 bands, increase in accuracy per increase in wavebands becomes asymptotic (e.g., Thenkabail et al., 2004a,b, 2012b). These studies, for example, show that when 40 Hyperion bands were used, the classification accuracies increased only by another 5% (from 90% with 20 bands to 95% with 40 bands). Here using 20 additional Hyperion bands (from 20 to 40) cannot be justified since the ground observation needed to train and test the algorithm will also increase exponential for 40 bands relative to 20. So, the key aim is to balance the higher classification accuracies with an optimal number of bands such as 20 instead too few or too many (e.g., 7 or 40). By doing so, we achieve a number of goals:

1. Increased classification accuracies with optimal number of bands.
2. Significantly reduced data redundancies with optimal number of bands.
3. Overcoming Hughes's phenomenon by using optimal number of bands (e.g., 20) in which observation data (ground data) to train and test the algorithms will be kept to reasonable levels.

## 9.5 Methods of Hyperspectral Data Analysis

Hyperspectral data analysis methods are broadly grouped under two categories (Bajwa and Kulkarni, 2012):

1. Feature extraction methods
2. Information extraction methods

Under each of the earlier two categories, specific unsupervised and supervised classification approaches exist (Figure 9.10) (Bajwa and Kulkarni, 2012; Plaza et al., 2012). Methods of classifying vegetation classes or crop types or vegetation species using HNBs are discussed extensively in this chapter and include unsupervised classification, supervised approaches, spectral angle mapper (SAM), artificial neural networks, and support vector machines (SVMs), multivariate or partial least square regressions (PLSR), and discriminant analysis (Thenkabail et al., 2012a).
Fundamental philosophies of hyperspectral data analysis involve two approaches:

1. Optimal hyperspectral narrowbands (OHNBs) where only a selective number of nonredundant bands are used (e.g., ~20 off Hyperion OHNBs are used).
2. Whole spectral analysis (WSA) where all the bands in the continuum (e.g., all 242 Hyperion bands in 400–2500 nm) are used.

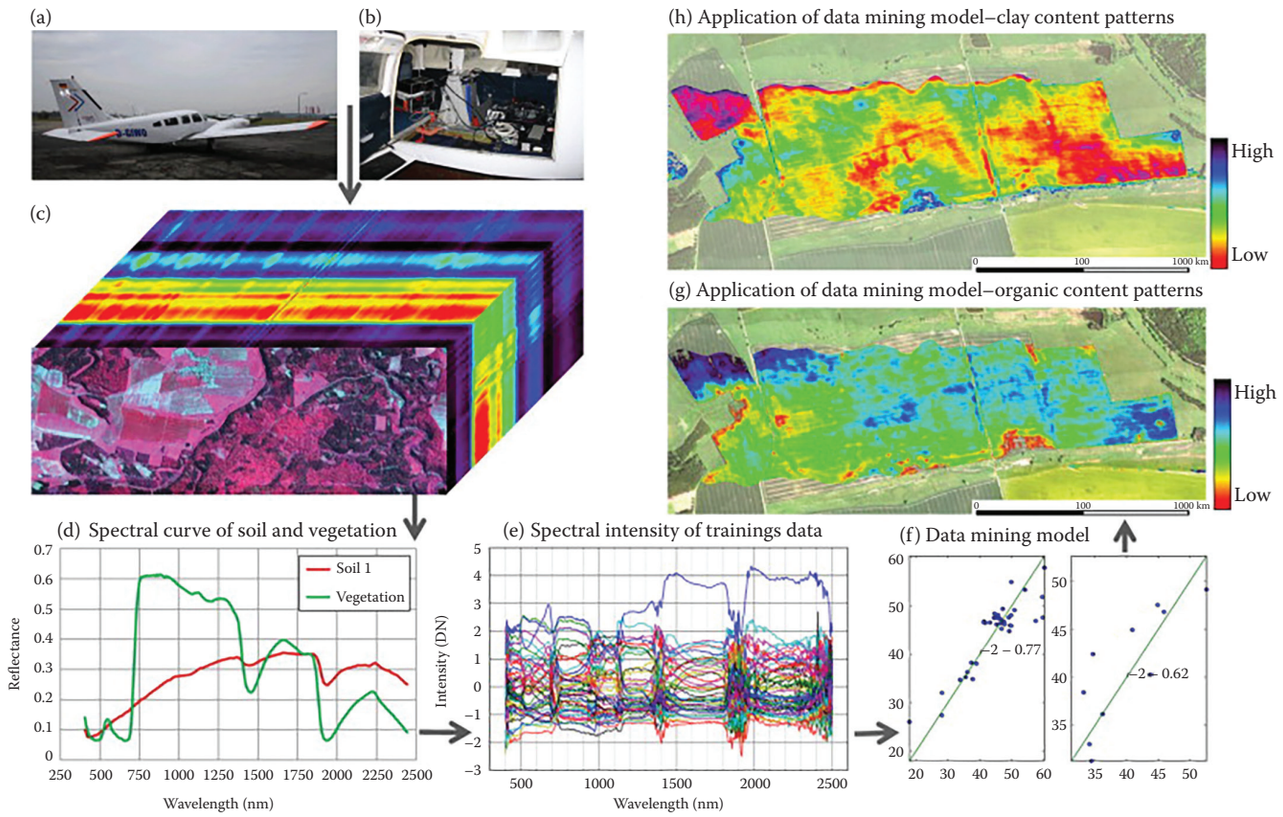


**FIGURE 9.9** Data mining 2. (a, b) Data mining and linked open data—New perspectives for data analysis in environmental research. Airborne hyperspectral AISA-Eagle/HAWK remote sensor mounted on Piper, (c) CIR-image from hyperspectral sensors of the AISA-EAGLE/HAWK (AISA-DUAL) 400–2500 nm with data cube, 367 spectral bands with 2 m recorded ground resolution, date of recording Mai 2012 with a Piper, Region Schäfertal—Bode Catchment, (d) Spectral curve of ground truth sampling points for soil and vegetation in the test site. (e) Spectral intensity curves of imaging hyperspectral data, (f) data mining model, (g) application of the best data mining model on airborne hyperspectral image data for quantification and recognition of organic content patterns, and (h) pattern of clay content. (From Lausch, A. et al., *Ecol. Model.*, 2014.)

## 9.6 Optimal Hyperspectral Narrowbands

Determining wavebands that are optimal for different studies requires a thorough study of these subjects. For example, the importance of the wavebands for different studies such as vegetation, geology, and water are all different. So, determining optimal OHNBs requires subject knowledge and considerable experience working with hyperspectral data. Based on the synthesis of the extensive studies conducted by Thenkabail et al. (2000, 2002, 2004a,b, 2012, 2013, 2014), the OHNBs for agriculture and vegetation studies are established and presented in Table 9.2. Each of these HNBs is identified for their importance in studying one or more of vegetation and crop biophysical and biochemical characteristics. Most of these bands are also very distinct from one another; so none of them are redundant. Using some combination of these bands will help better quantify the biophysical and biochemical characteristics of vegetation and agricultural crops (Alchanatis and Cohen, 2012; Pu, 2012). In the following sections and subsections, we will demonstrate how these HNBs are used in classifying, modeling, and mapping agricultural croplands and other vegetation.

Table 9.2 shows that over 400–2500 nm range of the spectrum, there are 28 bands (e.g., ~12% of the 242 Hyperion bands in 400–2500 nm range) that are optimal in the study of agriculture and vegetation. However, the redundant bands here (i.e., agriculture and vegetation applications) may be very useful in other applications such as geology (Ben-Dor, 2012). For example, the critical absorption bands for studying minerals like biotite, kaolinite, hematite, and others are shown in Table 9.3. Unlike the vegetation and cropland bands, the HNBs required for mineralogy are quite different (Vaughan et al., 2011; Slonecker, 2012).

The earlier fact clearly establishes the need to determine OHNBs that are application specific.

## 9.7 Hyperspectral Vegetation Indices

One of the most common, powerful, and useful form of feature selection methods for hyperspectral data is based on the calculation of HVIs (Clark, 2012; Colombo et al., 2012; Galvão, 2012;

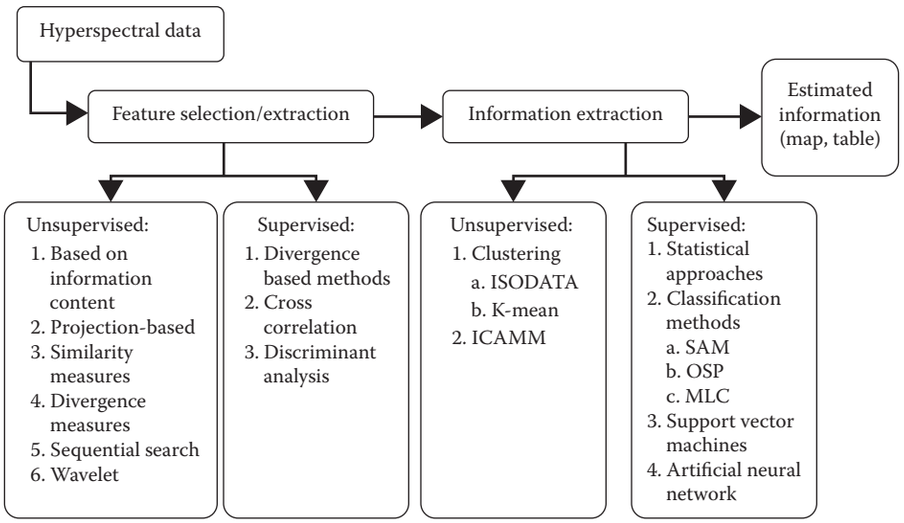


**FIGURE 9.10** Hyperspectral data analysis methods. (From Bajwa, S. and Kulkarni, S.S., Hyperspectral data mining, Chapter 4, in Thenkabail, P.S., Lyon, G.J., and Huete, A., *Hyperspectral Remote Sensing of Vegetation*, CRC Press/Taylor & Francis Group, Boca Raton, FL/London, U.K./New York, 2012, pp. 93–120.)

Gitelson, 2012a,b; Roberts, 2012). The HVIs achieve two important goals of hyperspectral data analysis:

1. Compute many specific targeted HVIs to help model biophysical and biochemical quantities.
2. Reduce the data volume (mine the data) to eliminate all redundant bands for a given application.

There are several approaches to deriving HVIs. These are briefly presented and discussed.

## 9.7.1 Two-Band Hyperspectral Vegetation Indices

The two-band hyperspectral vegetation indices (TBHVIs) are defined as follows (Thenkabail et al., 2000):

$$TBHVI_{ij} = \frac{(R_j - R_i)}{(R_j + R_i)} \quad (9.1)$$

where, i, j = 1 … N, with N = number of narrowbands. Hyperion 242 bands offer the possibility of 29,161 unique indices (242 * 242 = 58,564 – 242 = 58,322 divided by 2 resulting in $C^2_{242}$= 29,161; –242 because the values on the diagonal of matrix of 242 * 242 are unity, divided by 2 because the values above the diagonal of the matrix and below the diagonal of matrix are transpose of one another). However, as defined in Section 9.2.3, only 157 of the 242 Hyperion bands are useful after removing the wavebands in the atmospheric windows and those that are uncalibrated. This will still leave $C^2_{157}$= 12,246 unique TBHVIs.

Any one of the crop biophysical or biochemical quantity (e.g., biomass, leaf area index, nitrogen) is correlated with each one of the 12,246 TBHVIs (Stroppiana et al., 2012; Zhu et al., 2012). This will result for each crop variable (e.g., biomass) a total of 12,246 unique models, each providing an R-square. Figure 9.11 shows the contour plot of 12,246 R-square values plotted for (1) rice crop wet biomass with TBHVIs (Figure 9.11; above the diagonal) and (2) barley crop wet biomass with TBHVIs (Figure 9.11, below the diagonal). The areas with "bull's-eye" are regions of rich information having high R-square values, whereas the areas in gray are redundant bands with low R-square values. Based on these lambda ($\lambda_1$) versus lambda ($\lambda_2$) plots (Figure 9.11), the optimal waveband centers ($\lambda$) and widths ($\Delta\lambda$) are determined (Table 9.2). Table 9.2 shows the optimal wavebands ($\lambda$), wavebands centers ($\lambda$), and widths ($\Delta\lambda$) based on numerous studies (Thenkabail et al., 2000, 2002, 2004a,b, 2012, 2013, 2014), and a meta-analysis of these studies.

### 9.7.1.1 Refinement of Two-Band HVIs

Further refinement of each of the two-band HVIs (TBHVIs) is possible by computing (1) soil-adjusted versions of TBHVIs and (2) atmospheric corrected versions of TBHVIs. Interested readers can read more on this topic at Thenkabail et al. (2000).

## 9.7.2 Multi-Band Hyperspectral Vegetation Indices

The multi-band hyperspectral vegetation indices (MBHVIs) are computed as follows (Thenkabail et al., 2000; Li et al., 2012):

$$MBHVI_i = \sum_{j=1}^{N} a_{ij} R_j \quad (9.2)$$

where

$MBHVI_i$ is the crop variable i
R is the reflectance in bands j (j = 1 – N with N = 242 for Hyperion)
a is the coefficient for reflectance in band j for ith variable

**TABLE 9.2** Optimal (Nonredundant) Hyperspectral Narrowbands to Study Vegetation and Agricultural Crops[a, b, c]

| Waveband Number (#) | Waveband Range (λ) | Waveband Center (λ) | Waveband Width (Δλ) | Importance and Physical Significance of Waveband in Vegetation and Cropland Studies |
|---|---|---|---|---|
| A. Ultraviolet | | | | |
| 1 | 373–377 | 375 | 5 | fPAR, leaf water: fraction of photosynthetically active radiation (fPAR), leaf water content |
| B. Blue bands | | | | |
| 2 | 403–407 | 405 | 5 | Nitrogen, Senescing: sensitivity to changes in leaf nitrogen reflectance changes due to pigments is moderate to low. Sensitive to senescing (yellow and yellow green leaves). |
| 3 | 491–500 | 495 | 10 | Carotenoid, Light use efficiency (LUE), Stress in vegetation: Sensitive to senescing and loss of chlorophyll\browning, ripening, crop yield, and soil background effects |
| C. Green bands | | | | |
| 4 | 513–517 | 515 | 5 | Pigments (Carotenoid, Chlorophyll, anthocyanins), Nitrogen, Vigor: positive change in reflectance per unit change in wavelength of this visible spectrum is maximum around this green waveband |
| 5 | 530.5–531.5 | 531 | 1 | Light use efficiency (LUE), Xanophyll cycle, Stress in vegetation, pest and disease: Senescing and loss of chlorophyll\browning, ripening, crop yield, and soil background effects |
| 6 | 546–555 | 550 | 10 | Chlorophyll: Total chlorophyll; Chlorophyll/carotenoid ratio, vegetation nutritional and fertility level; vegetation discrimination; vegetation classification |
| 7 | 566–575 | 570 | 10 | Pigments (Anthocyanins, Chlorophyll), Nitrogen: negative change in reflectance per unit change in wavelength is maximum as a result of sensitivity to vegetation vigor, pigment, and N. |
| D. Red bands | | | | |
| 8 | 676–685 | 680 | 10 | Biophysical quantities and yield: leaf area index, wet and dry biomass, plant height, grain yield, crop type, crop discrimination |
| E. Red-edge bands | | | | |
| 9 | 703–707 | 705 | 5 | Stress and chlorophyll: Nitrogen stress, crop stress, crop growth stage studies |
| 10 | 718–722 | 720 | 5 | Stress and chlorophyll: Nitrogen stress, crop stress, crop growth stage studies |
| 11 | 700–740 | 700–740 | 700–740 | Chlorophyll, senescing, stress, drought: first-order derivative index over 700–740 nm has applications in vegetation studies (e.g., blue-shift during stress and red-shift during healthy growth) |
| F. Near infrared (NIR) bands | | | | |
| 12 | 841–860 | 850 | 20 | Biophysical quantities and yield: LAI, wet and dry biomass, plant height, grain yield, crop type, crop discrimination, total chlorophyll |
| 13 | 886–915 | 900 | 20 | Biophysical quantities, Yield, Moisture index: peak NIR reflectance. Useful for computing crop moisture sensitivity index, NDVI; biomass, LAI, Yield. |
| G. Near infrared (NIR) bands | | | | |
| 14 | 961–980 | 970 | 20 | Plant moisture content Center of moisture sensitive "trough"; water band index, leaf water, biomass; |
| H. Far near infrared (FNIR) bands | | | | |
| 15 | 1073–1077 | 1075 | 5 | Biophysical and biochemical quantities: leaf area index, wet and dry biomass, plant height, grain yield, crop type, crop discrimination, total chlorophyll, anthocyanin, carotenoids |
| 16 | 1178–1182 | 1080 | 5 | Water absorption band |
| 17 | 1243–1247 | 1245 | 5 | Water sensitivity: water band index, leaf water, biomass. Reflectance peak in 1050–1300 nm |
| I. Early short-wave infrared (ESWIR) bands | | | | |
| 18 | 1448–1532 | 1450 | 5 | Vegetation classification and discrimination: ecotype classification; plant moisture sensitivity. Moisture absorption trough in early short wave infrared (ESWIR) |
| 19 | 1516–1520 | 1518 | 5 | Moisture and biomass: A point of most rapid rise in spectra with unit change in wavelength in SWIR. Sensitive to plant moisture. |
| 20 | 1648–1652 | 1650 | 5 | Heavy metal stress, Moisture sensitivity: Heavy metal stress due to reduction in Chlorophyll Sensitivity to plant moisture fluctuations in ESWIR. Use as an index with 1548 or 1620 or 1690 nm. |
| 21 | 1723–1727 | 1725 | 5 | Lignin, biomass, starch, moisture: sensitive to lignin, biomass, starch Discriminating crops and vegetation. |
| J. Far short-wave infrared (FSWIR) bands | | | | |
| 22 | 1948–1952 | 1950 | 5 | Water absorption band: highest moisture absorption trough in FSWIR. Use as an index with any one of 2025, 2133, and 2213 nm Affected by noise at times. |
| 23 | 2019–2027 | 2023 | 8 | Litter (plant litter), lignin, cellulose: litter-soil differentiation: moderate to low moisture absorption trough in FSWIR. Use as an index with any one of 2025, 2133, and 2213 nm |

(*Continued*)

**TABLE 9.2 (*Continued*)** Optimal (Nonredundant) Hyperspectral Narrowbands to Study Vegetation and Agricultural Crops[a, b, c]

| Waveband Number (#) | Waveband Range (λ) | Waveband Center (λ) | Waveband Width (Δλ) | Importance and Physical Significance of Waveband in Vegetation and Cropland Studies |
|---|---|---|---|---|
| 24 | 2131–2135 | 2133 | 5 | Litter (plant litter), lignin, cellulose: typically highest reflectivity in FSWIR for vegetation. Litter- soil differentiation |
| 25 | 2203–2207 | 2205 | 5 | Litter, lignin, cellulose, sugar, starch, protein; Heavy metal stress: typically, second highest reflectivity in FSWIR for vegetation. Heavy metal stress due to reduction in Chlorophyll |
| 26 | 2258–2266 | 2262 | 8 | Moisture and biomass: moisture absorption trough in far short-wave infrared (FSWIR). A point of most rapid change in slope of spectra based on land cover, vegetation type, and vigor. |
| 27 | 2293–2297 | 2295 | 5 | Stress: sensitive to soil background and plant stress |
| 28 | 2357–2361 | 2359 | 5 | Cellulose, protein, nitrogen: sensitive to crop stress, lignin, and starch |

*Sources:* Modified and adopted from Thenkabail, P.S. et al., *Remote Sens. Environ*., 71, 158, 2000; Thenkabail, P.S. et al. (2002); Thenkabail, P.S. et al., *Remote Sens. Environ*., 90, 23, 2004a; Thenkabail, P.S. et al., *Remote Sens. Environ*., 91, 354, 2004b; Thenkabail et al. (2012, 2013); Thenkabail, P.S. et al., *Photogramm. Eng. Remote Sens*., 80, 697, 2014.

[a] Most hyperspectral narrowbands (HNBs) that adjoin one another are highly correlated for a given application. Hence from a large number of HNBs, these non-redundant (optimal) bands are selected.

[b] These optimal HNBs are for studying vegetation and agricultural crops. When we use some or all of these wavebands, we can attain highest possible classification accuracies in classifying vegetation categories or crop types.

[c] Wavebands selected here are based on careful evaluation of large number of studies.

**TABLE 9.3** Subpixel Mineral Mapping of a Porphyry Copper Belt Using EO-1 Hyperion Data

| Hyperion Band (#) | Wavelength (nm) | Feature | Minerals | Mineral Characteristic |
|---|---|---|---|---|
| 210, 217 | 2254, 2324 | Absorption | Biotite | Potassic-biotitic alteration zone |
| 205 | 2203 | Absorption | Muscovite and illite | Al–OH vibration in minerals with muscovite deeper absorption than illite |
| 201, 205 | 2163, 2203 | Absorption | Kaolinite | Al–OH vibration |
| 14, 79, 205 | 487, 932, 2203 | Absorption | Goethite | |
| 14, 53, 205 | 487, 884, 2203 | Absorption | Hematite | |
| 79211205 | 932, 2264, 2203 | Absorption | Jarosite | |
| 201 | 2163 | Absorption | Pyrophyllite | Al–OH and Mg–OH |
| 218 | 2335 | Absorption | Chlorite | Al–OH and Mg–OH |

*Source:* Adopted and modified from information in manuscript by Hosseinjani Zadeh, M. et al., *Adv. Space Res.*, 53, 440, 2014.

The process of modeling involves running stepwise linear regression models (e.g., using MAXR algorithm in Statistical Analysis System (SAS, 2009) with any one biophysical or biochemical variable (e.g., biomass) as dependent variable and the numerous HNBs as independent variables (e.g., 157 of the 242 useful bands of Hyperion). In this modeling approach, we will get the best one-band, two-band, three-band, and so on to best n-band model. The best one-band model is the one in which the biomass (taken as example) has highest R-square value with a single band out of the total 157 Hyperion HNBs. Then, we obtain the best two-band model, in which two HNBs provide a best R-square value with biomass. Similarly, the best three-band, best four-band, and best n-band (e.g., all 157 Hyperion bands) models are obtained, even though, theoretically, all 157 bands can be involved in providing a 157-band biomass model that is usually meaningless due to over-fitting of data. However, a plot of R-square values (y-axis) versus the number of bands (x-axis) will show us when an increase in R-square values with the addition of wavebands becomes asymptotic. Alternatively, we can also consider additional bands, when there is at least an increase of 0.03 or higher in R-square value when additional bands are added. So, the approach we can use is to look at one-band model and see its R-square. Then, when two-band model increases R-square value by at least 0.03 (a threshold we can set), then consider the two-band model; otherwise, retain the one-band model as final. At some stage, we will notice that addition of a band does not increase R-square value by more than 0.03. Typically, we have noticed that anywhere between 3 and 10 HNBs explain optimal variability in most agricultural crop and vegetation variables. Beyond these 3–10 bands, the increase in R-square per increase in band is insignificant or asymptotic. However, which 3–10 bands within 400–2500 nm will, often, vary is based on the type of crop variable.

Through MBHVIs, we can establish the following:

1. How many HNBs are required to achieve an optimal R-square for any biophysical or biochemical quantity?
2. Which HNBs are involved in providing optimal R-square?
3. Through this process, we can determine which are important HNBs and which are redundant. However, the best approach to achieve this is by a study conducted for many crops, involving several crop variables, and based on data from multiple sites and years. Table 9.2 provides one such summary.

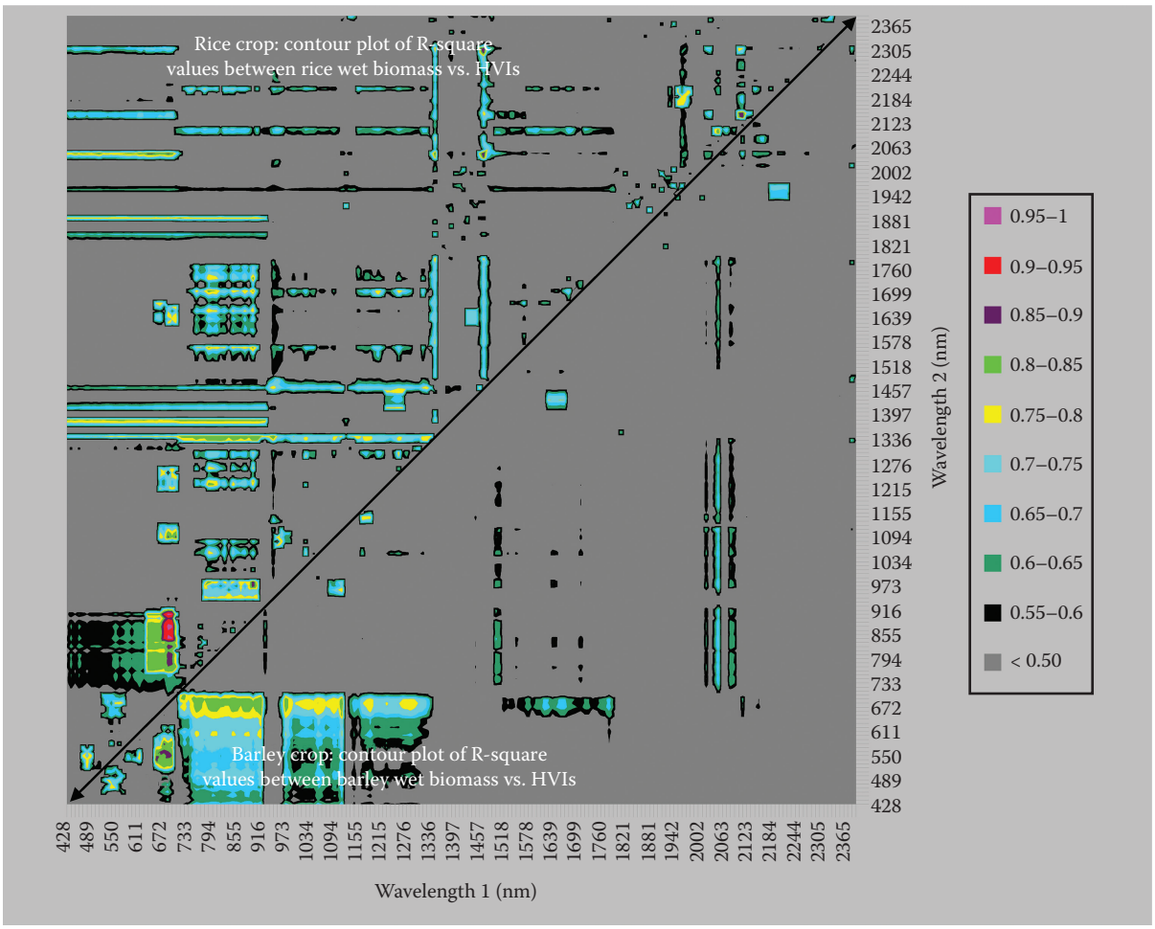


**FIGURE 9.11** Lambda (λ) versus Lambda (λ) plot of R-square values between wet biomass and hyperspectral vegetation indices (HVIs) for the rice crop (above the diagonal) and barley crop (below the diagonal).

These MBHVIs take advantage of the key absorption and reflective portions of the spectrum (e.g., Figure 9.12; [Gnyp et al., 2014]). Taking advantage of four HNBs, two reflective (900 and 1050 nm) and two absorptive (955 and 1220 nm), Gnyp et al. constitute an MBHVI (Equation 9.1). In their paper, Gnyp et al. (2014) clearly demonstrate the significantly higher R-square values provided by such a multiband HVIs when compared with other two-band HVIs (e.g., in Figure 9.13, GnyLi has a much higher R-square value relative to other indices). Interesting and maybe noteworthy that while the typical saturation effect (lack of sensitivity) at higher biomass amounts is still present, it is evidently somewhat less severe with GnyLi than the others (except REP but it has lower r2). Also, research by Thenkabail et al. (2004a, b), Mariotto et al. (2013), and Marshall and Thenkabail (2014) has demonstrated that anywhere between 3 and 10 HNBs involved in multiband HVIs explain greatest variability in modeling various biophysical and biochemical quantities for various agricultural crops.

However, it needs to be noted that the specific band centers and band widths are not as definitive as shown in Figure 9.12 or/and Equation 9.1. This is because, with crop type and crop growing conditions, the specific reflective maxima (900 and 1050 nm) and reflective minima (955 and 1220 nm) shown in Figure 9.12 and Equation 9.1 can vary. For example, the moisture absorption maxima can be at 750, 760, 770, or 780 nm (Thenkabail et al., 2012, 2013) or can be at 755 nm as shown in Figure 9.12 and Equation 9.1. As a result, we performed meta-analysis of a number of papers to come with the recommendations of HNB centers and HNB widths (Table 9.2) that are optimal for use in HVI computations across crops and vegetation.

$$\text{GnyLi} = \frac{R_{900} \times R_{1050} - R_{955} \times R_{1220}}{R_{900} \times R_{1050} + R_{955} \times R_{1220}} \tag{9.3}$$

## 9.8 The Best Hyperspectral Vegetation Indices and Their Categories

Based on extensive research over the last decade (Thenkabail et al., 2000, 2002, 2004a,b, 2012, 2013, 2014), six distinct categories of two-band TBHVIs (Table 9.4) are considered most significant and important in order to study specific biophysical and biochemical quantities of agriculture and vegetation. Author recommends

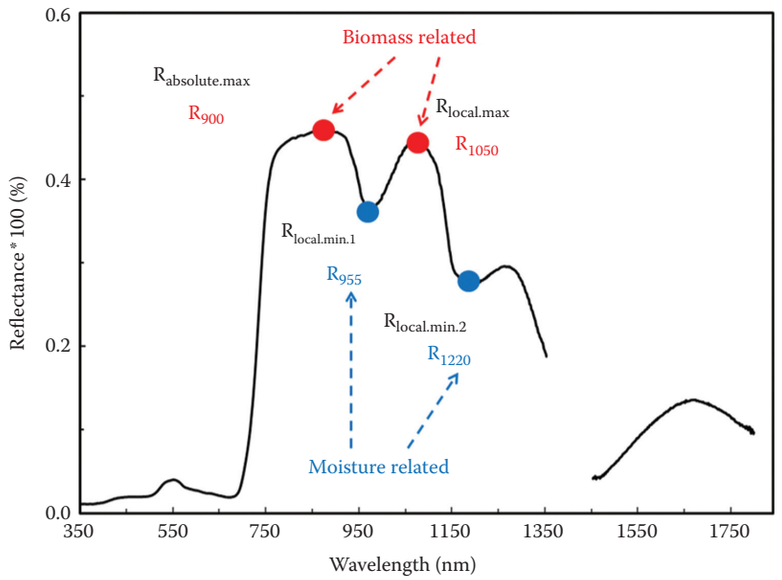


**FIGURE 9.12** New index. Development and implementation of a multiscale biomass model using hyperspectral vegetation indices for winter wheat in the North China Plain. Reflectance of winter wheat and its characteristic peaks and troughs with the reflectance maxima and minima in the NIR and SWIR domains. These peaks were used to compute the VI GnyLi. R is the reflectance value (%) at a specific wavelength (nm). (From Gnyp, M.L. et al., *Int. J. Appl. Earth Obs. Geoinf.*, 33, 232, 2014.)

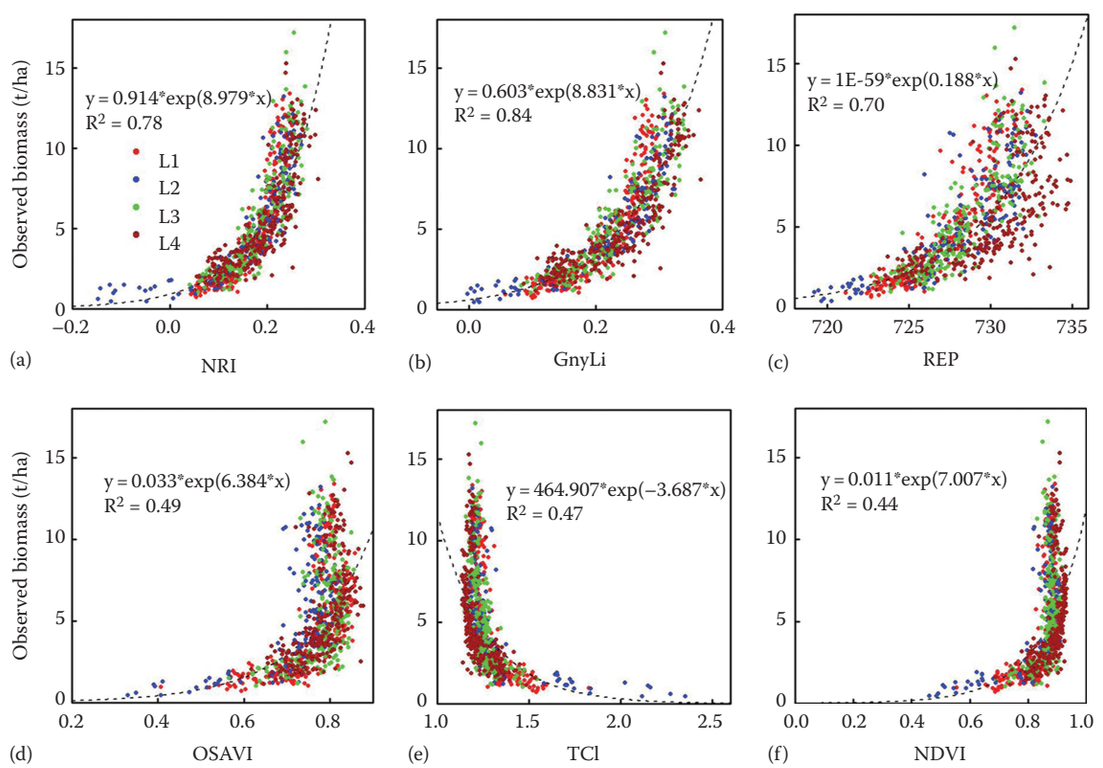


**FIGURE 9.13** Observed biomass versus various HVIs and also GnyLi (see Figure 9.20). R is the reflectance value (%) at a specific wavelength (nm). (From Gnyp, M.L. et al., *Int. J. Appl. Earth Obs. Geoinf.*, 33, 232, 2014.)

**TABLE 9.4** Hyperspectral Vegetation Indices or HVIs

| Band Number (#) | Hyperspectral Narrowband ($\lambda_1$) | Bandwidth ($\Delta\lambda_1$) | Hyperspectral Narrowband ($\lambda_2$) | Bandwidth ($\Delta\lambda_2$) | Hyperspectral Vegetation Index (HVI) | Best Index Under Each Category |
|---|---|---|---|---|---|---|
| 1. Hyperspectral biomass and structural indices (HBSIs) (to best study biomass, LAI, plant height, and grain yield) | | | | | | |
| HBSI1 | 855 | 20 | 682 | 5 | (855 – 682)/(855 + 682) | HBSI: Hyperspectral biomass and structural index |
| HBSI2 | 910 | 20 | 682 | 5 | (910 – 682)/(910 + 682) | |
| HBSI3 | 550 | 5 | 682 | 5 | (550 – 682)/(550 + 682) | |
| 2. Hyperspectral biochemical indices (HBCIs) (pigments like carotenoids, anthocyanins as well as Nitrogen, chlorophyll) | | | | | | |
| HBCI8 | 550 | 5 | 515 | 5 | (550 – 515)/(550 + 515) | HBCI: Hyperspectral biochemical index |
| HBCI9 | 550 | 5 | 490 | 5 | (550 – 490)/(550 + 490) | |
| 3. Hyperspectral Red-edge indices (HREIs) (to best study plant stress, drought) | | | | | | |
| HREI14 | 700 – 740 | 40 | First-order derivative integrated over red-edge. | | | HREI: Hyperspectral red-edge index |
| HREI15 | 855 | 5 | 720 | 5 | (855 – 720)/(855 + 720) | |
| 4. Hyperspectral water and moisture indices (HWMIs) (to best study plant water and moisture) | | | | | | |
| HWMI17 | 855 | 20 | 970 | 10 | (855 – 970)/(855 + 970) | HWMI: Hyperspectral water and moisture index |
| HWMI18 | 1075 | 5 | 970 | 10 | (1075 – 970)/(1075 + 970) | |
| HWMI19 | 1075 | 5 | 1180 | 5 | (1075 – 1180)/(1075 + 1180) | |
| HWMI20 | 1245 | 5 | 1180 | 5 | (1245 – 1180)/(1245 + 1180) | |
| 5. Hyperspectral light-use efficiency index (HLEI) (to best study light use efficiency or LUE) | | | | | | |
| HLUE24 | 570 | 5 | 531 | 1 | (570 – 531)/(570 + 531) | HLEI: Hyperspectral light-use efficiency index |
| 6. Hyperspectral lignin cellulose index (HLCI) (to best study plant lignin, cellulose, and plant residue) | | | | | | |
| HLCI25 | 2205 | 5 | 2025 | 1 | (2205 – 2025)/(2205 + 2025) | HLCI: Hyperspectral lignin cellulose index |

*Sources:* Modified and adopted from Thenkabail, P.S. et al., *Photogramm. Eng. Remote Sens.*, 80, 697, 2014.
*Note:* Also see wavebands in Table 9.2 used to derive these indices.

that in future, researchers use these HVIs, derived using HNBs, for their studies to quantify and model biophysical and biochemical quantities of various agricultural crops and vegetation of different types. The values of two such indices are illustrated. These are (1) hyperspectral biomass and structural index 1 (HBSI1; Thenkabail et al., 2014), derived using the Hyperion bands centered around 855 and 682 nm (each with 10 nm width), is applied to an agricultural area to determine biomass (Figure 9.14); and (2) photochemical reflectance index (PRI) for stress detection (e.g., Figure 9.15; Middleton et al., 2012). The importance of wavebands in computing the indices for various biophysical and biochemical is illustrated in Figure 9.16. Reader is encouraged to compare Figure 9.15 with Table 9.4 and Table 9.2 for better understanding of HNBs (Table 9.2), HVIs (Table 9.4), and their importance (Figure 9.16) in studies pertaining to crops and vegetation.

## 9.9 Whole Spectral Analysis

A number of chapters discuss the usefulness and utility of using whole spectra (e.g., continuous and entire spectra over 400–2500 nm) for analysis using such methods as PLSR, wavelet analysis, continuum removal, SAM, and spectral matching techniques (SMTs) (Thenkabail et al., 2012).

### 9.9.1 Spectral Matching Techniques

SMTs (Thenkabail et al., 2007) involves the following:

1. *Ideal or target spectral library creation*: Collecting ideal or target spectra (e.g., specific crops, specific species, specific mineral) and creating a spectral library.
2. Class spectra collection.
3. Matching class spectra with ideal spectra to identify and label classes.

The principal approach in SMT is to match the shape or the magnitude or (preferably) both to an ideal or target spectrum (pure class or "end member"). Thenkabail et al. (2007) proposed and implemented SMT for multitemporal data illustrated later (Figure 9.17). The qualitative pheno-SMT approach concept remains the same for hyperspectral data (replace the number of bands of temporal data with the number of hyperspectral bands).

The quantitative SMTs consist of (Thenkabail et al., 2007) (1) spectral correlation similarity—a shape measure; (2) spectral similarity value—a shape and magnitude measure; (3) Euclidian distance similarity—a distance measure; and (4) modified spectral angle similarity—a hyper angle measure.

### 9.9.2 Continuum Removal through Derivative Hyperspectral Vegetation Indices

The derivative hyperspectral vegetation indices (DHVIs) are computed by integrating index over a certain wavelength (e.g., 600–700 nm or 700–760 nm). The equation is

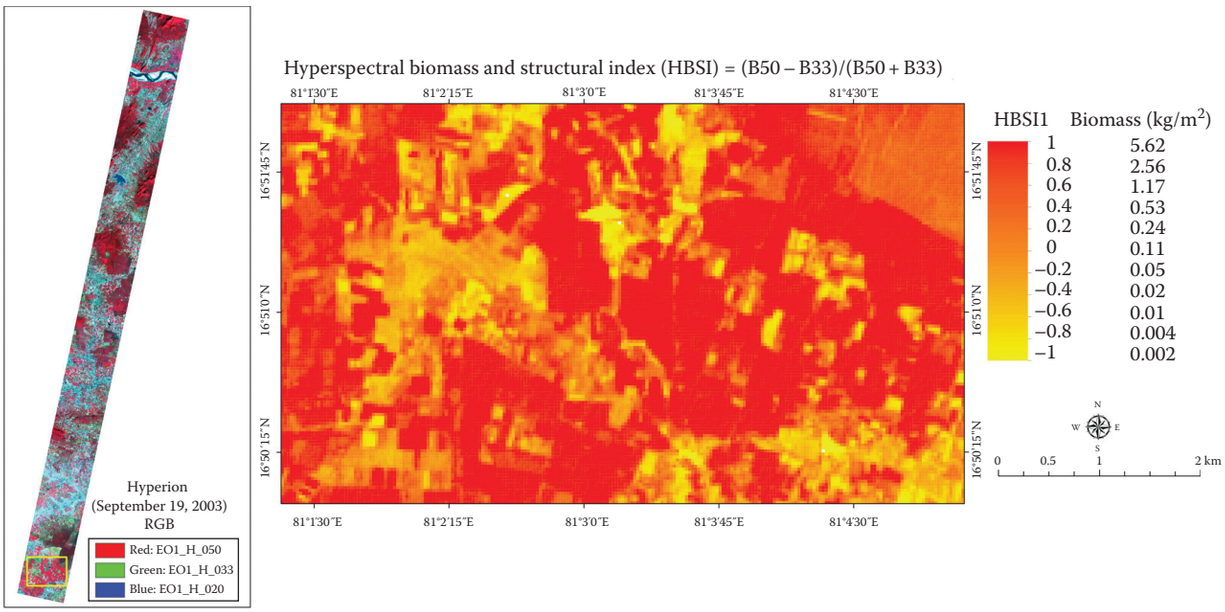


**FIGURE 9.14** Spatial depiction of a hyperspectral biomass and structural index 1 (HBSI1) as applied to an agricultural area. One of the HVIs (HBSI1) in mapping wet biomass for a study area using Hyperion hyperspectral data. The red area in the z-scale can be stretched further to show better biomass variability with change in HBSI1. For example, HBSI1 0.4 = 0.53 and HBSI 0.6 = 1.16, HBSI1 0.8 = 2.56, and HBSI1 = 5.62. The current stretch does not adequately show these differences (as much of the higher end is in red). However, if we stretch between HBSI1 from 0.4 to 1.0, then the biomass differences in this HBSI1 range, which is 0.53–5.62, will show up in better contrast. The relationship between HBSI1 and biomass is nonlinear due to saturation of indices at the higher end of the biomass. However, this saturation is much lower for hyperspectral index like HBSI1 when compared to broadband NDVI.

$$\text{DHVI} = \sum \frac{\lambda_n(\rho'(\lambda_i) - (\rho'(\lambda j)}{\lambda_1 \Delta\lambda_I} \tag{9.4}$$

where

i and j are band numbers

λ is the center of wavelength

The process of obtaining DHVI value for 600–700 nm is as follows: (1) DHVI1 = lambda 1 (e.g., $\lambda_1$ = 600 nm) versus lambda 2 (e.g., $\lambda_2$ = 610 nm). The difference in the reflectivity of these two bands is then divided by their bandwidth ($\Delta\lambda_I$ = 10 nm) and (2) DHVI2 = the process is repeated for lambda 1 (e.g., $\lambda_1$ = 610 nm) versus lambda 2 (e.g., $\lambda_2$ = 620 nm). The difference in reflectivity of these two bands is then divided by their bandwidth ($\Delta\lambda_I$ = 10 nm) and (3) DHVIn = so on to lambda 1 (e.g., $\lambda_1$ = 690 nm) versus lambda 2 (e.g., $\lambda_2$ = 700 nm). The difference in reflectivity of these two bands is then divided by their bandwidth ($\Delta\lambda_I$ = 10 nm). Finally, add DHVI1, DHVI2, and so on to DHVIn to get single an integrated DHVI value over the entire 600–700 nm range.

The DHVIs can be derived over various wavelengths such as 400–2500 nm, 500–600 nm, 600–800 nm, and any other wavelength you find useful for the particular application. There are opportunities to further investigate the significance of DHVIs over different wavelengths for a wide array of applications.

## 9.10 Principal Component Analysis

Another common, powerful, and useful feature selection method for hyperspectral data analysis is PCA. The PCA performs following functions:

1. *Reduces data volumes*: This happens since the PCA generates numerous principal components (PCs) (as many as the number of wavebands), but the first few PCs explain almost all the variability of data. The first PC (PC1) explains the highest, followed by the other. Since each PC is constituted based on the information from all the bands (e.g., PC1 = factor loading for band 1 * band 1 reflectivity + ⋯ + factor loading for band n * band n reflectivity), the PCs have the power of hyperspectral bands, but does not have all the redundancy of the same.
2. *Provides a new single band of information* (e.g., PC1, PC2), each of which (e.g., PC1) actually has the information derived from all the HNBs. These new bands of information (e.g., PC1) can then be used to classify an area (e.g., to establish crop types) or used to model crop biophysical or biochemical quantities.
3. *The power of PCs* can be used to discriminate crop types, or land cover themes, or species (e.g., Figure 9.18).

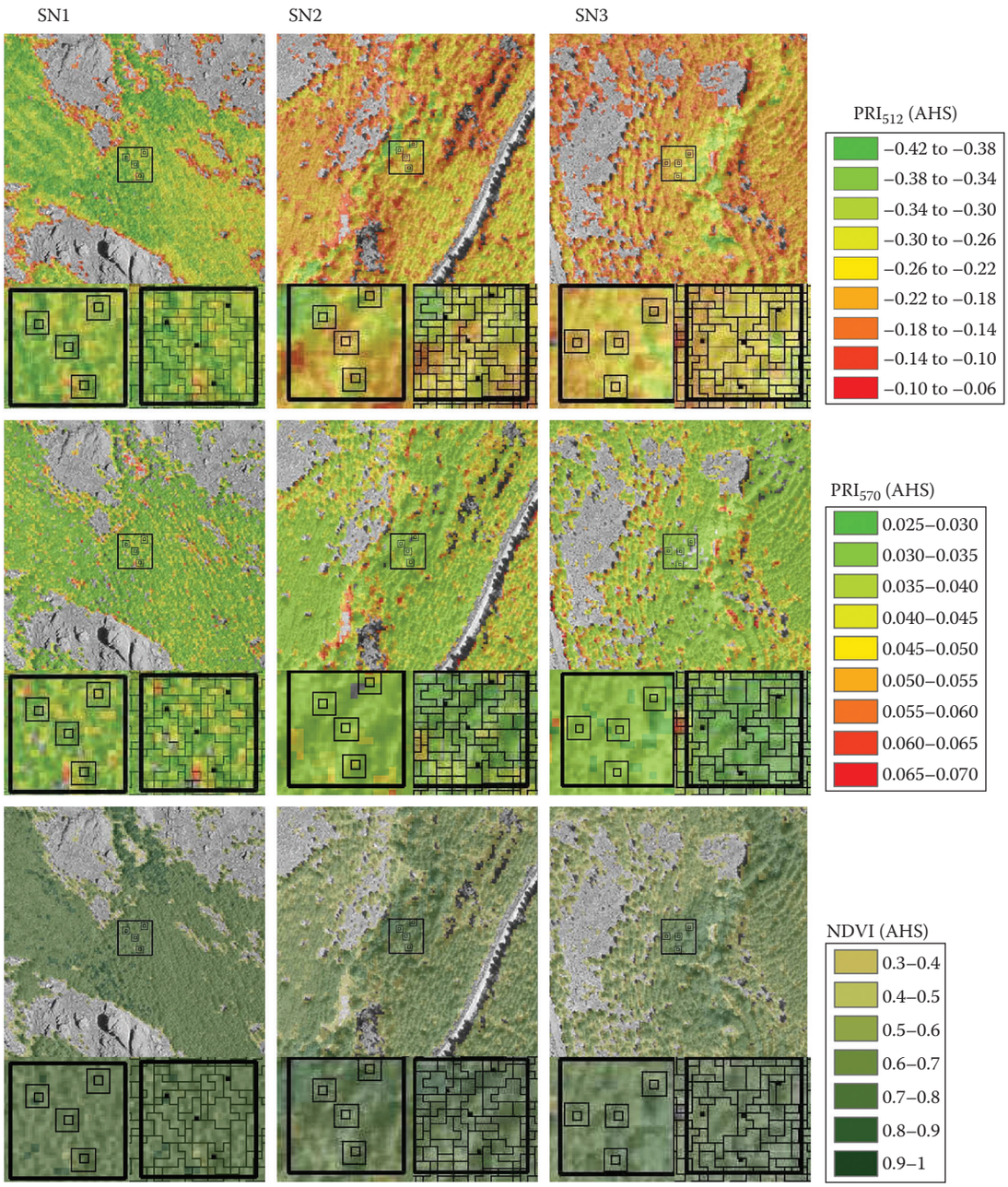


**FIGURE 9.15** Assessing structural effects on photochemical reflectance index (PRI) for stress detection in conifer forests. $PRI_{512}$, $PRI_{570}$, and NDVI obtained from the AHS airborne sensor from three study areas of *Pinus nigra* with different levels of stress: SN1, SN2, and SN3. At the bottom of each image, two zoom images of a central plot, one pixel based displaying 1 × 1 and 3 × 3 resolutions and the other at object level. *Note*: $PRI_{512}$ is a normalized index involving a waveband centered at 512 and 531 nm, whereas $PRI_{570}$ is a normalized index involving a waveband centered at 570 and 531 nm. Airborne hyperspectral scanner (AHS) (Sensytech Inc., currently Argon St. Inc., Ann Arbor, MI) acquiring 2 m spatial resolution imagery in 38 bands in the 0.43–12.5 μm spectral range. (From Hernández-Clemente, R. et al., *Adv. Space Res.*, 53, 440, 2011.)

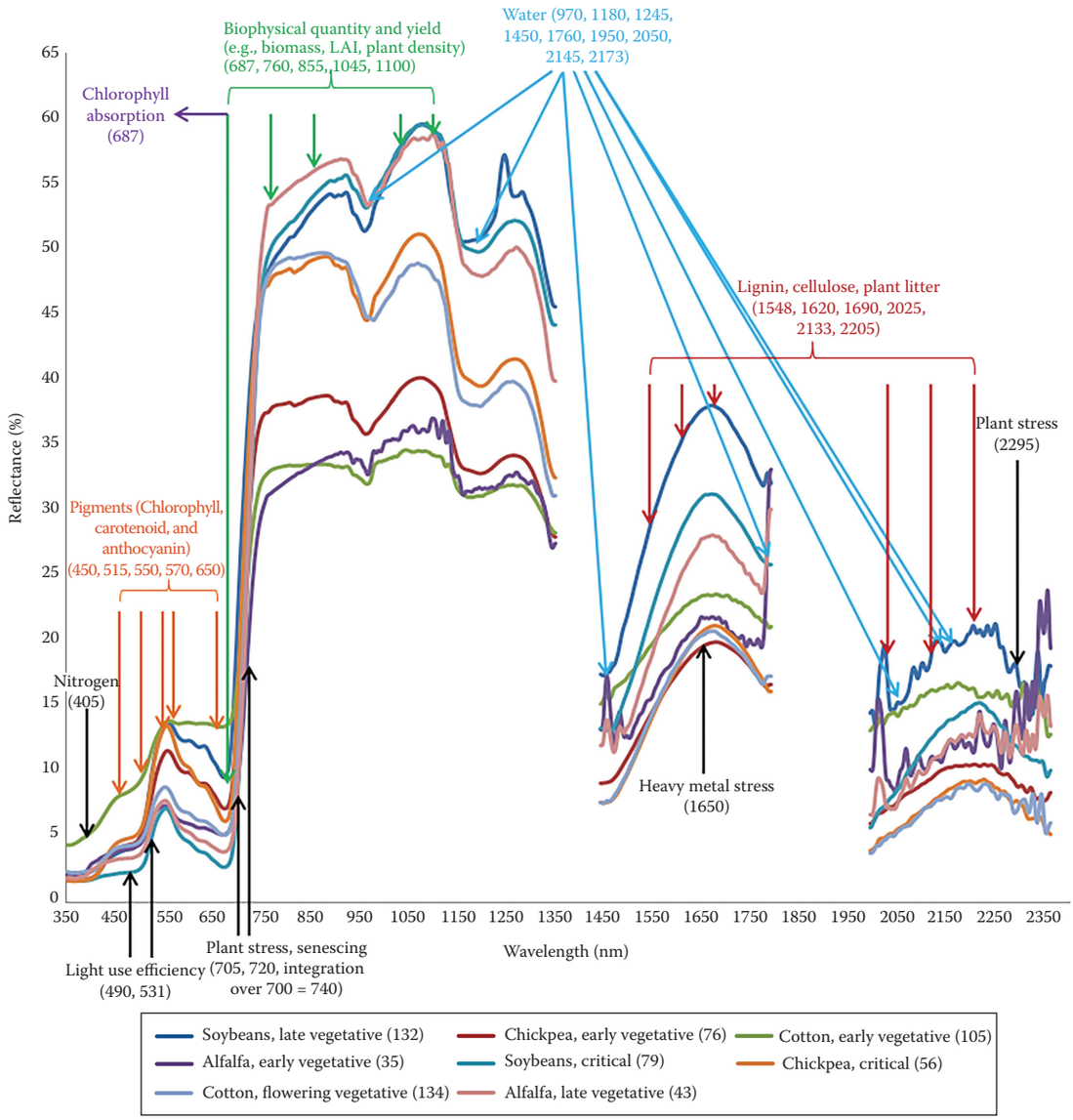


**FIGURE 9.16** Importance of various portions of hyperspectral data in characterizing biophysical and biochemical quantities of crops and vegetation.

## 9.11 Spectral Mixture Analysis of Hyperspectral Data

Hyperspectral data have great ability to distinguish specific objects based on their unique signatures. For example, wheat versus barley crops are distinguished based on the spectral reflectivity in two HNBs, each of 10 nm wide, and centered at 687 and 855 nm (e.g., Figure 9.19). However, often, we find multiple objects or classes within a pixel. In situations like that, we will need to perform spectral mixture analysis (SMA) and an independent component analysis, in order to unmix the spectral signatures within each pixel.

The reference spectra for SMA are derived from "end members" (e.g., Figure 9.20). Once all the materials in the image are identified, then it is possible to use linear or nonlinear spectral unmixing to find out how much of each material is in each pixel.

The concept of unmixing hyperspectral data is illustrated by showing Hyperion unmixing of (1) vegetation fractional cover in Figure 9.21 and (2) minerals in Figure 9.22. Subpixel mineral mapping of a porphyry copper belt using EO-1 Hyperion data in Figure 9.23 involved mineral spectra extracted from Hyperion compared to convolved spectra from field samples and reference library spectra (Figures 9.20 and 9.21; Hosseinjani Zadeh et al., 2014). Extensive discussions on linear and nonlinear SMAs can be found in Plaza et al. (2012).

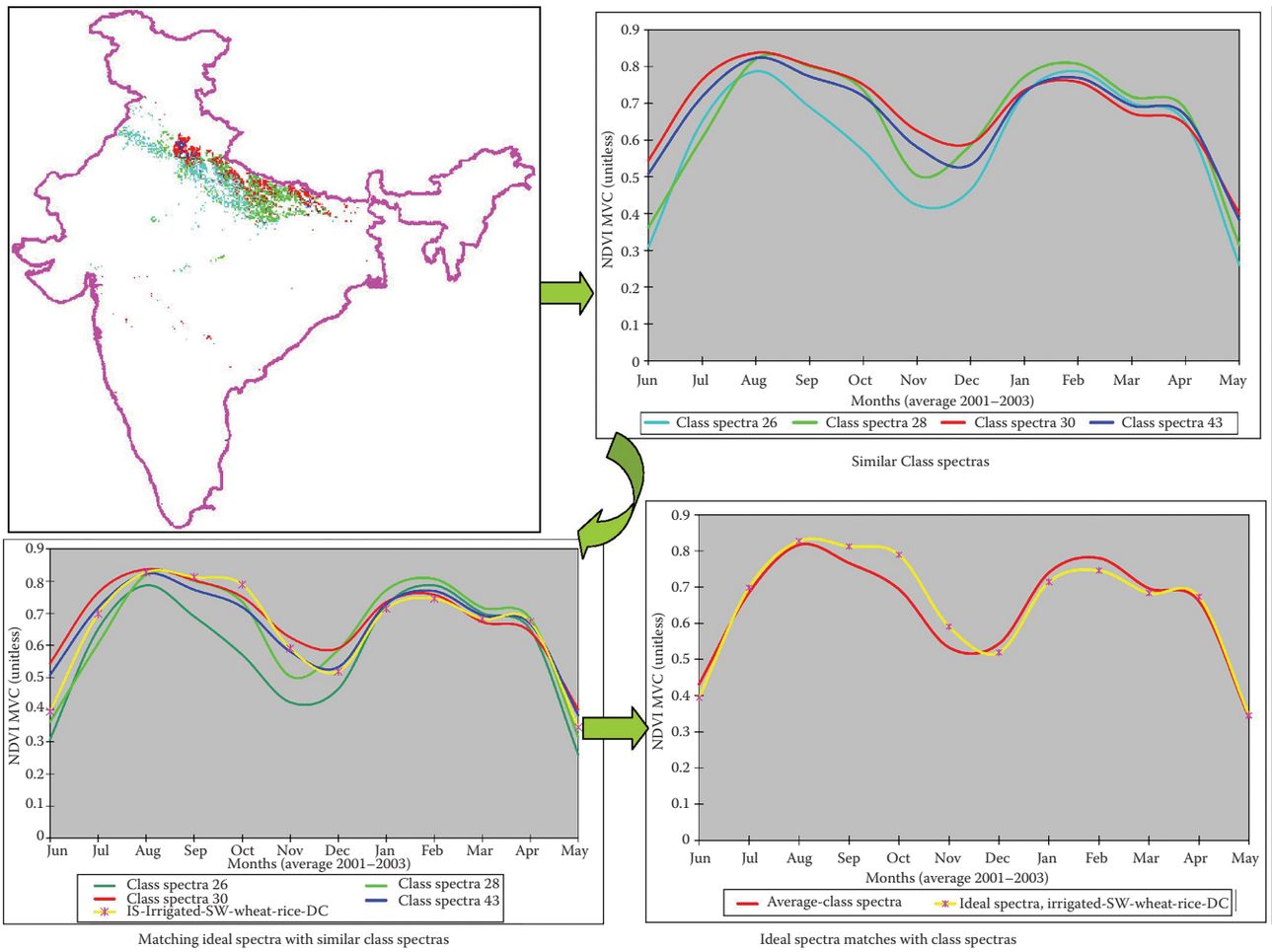


**FIGURE 9.17** Pheno-spectral matching technique (SMTs). In SMTs, the class temporal profiles (NDVI curves) are matched with the ideal temporal profile (quantitatively based on temporal profile similarity values) in order to group and identify classes as illustrated for a rice class in this figure. Illustration of double-crop (DC) irrigation. The NDVI spectra of the four classes (C-26, C-28, C-30, and C-43) of DC irrigation are "matched" with ideal spectra (shaded in yellow) for the same. This is a qualitative illustration of SMTs. For quantitative methods, refer to Thenkabail et al. 2007.

## 9.12 Support Vector Machines

SVMs are a machine learning supervised classification approach. Unlike the feature selection approach, data dimensionality is not an issue here. Any number of bands can be used. The process involves supervised training of classes, based on sufficient and accurate knowledge of the class (e.g., ground data), where one can use all or some of the hyperspectral bands to train the algorithm. Once the algorithm is sufficiently trained, it can be run on rest of the data to gather the same class occurring in other areas. Figure 9.24a shows the classification performed using all 272 AISA hyperspectral bands based on SVM algorithm. In Figure 9.24b, the same classification is performed using only 51 of the most important AISA hyperspectral bands. Results of the 51-band classification output (Figure 9.24b) are comparable to 272-band classification output (Figure 9.24a) in most areas; there is significant uncertainty in the northern portion of the image. Studies have shown that by using only 1% of training pixels per class, almost 90% overall classification accuracies are obtained using SVM methods (Bajwa and Kulkarni, 2012; Ramsey III and Rangoonwala, 2012).

## 9.13 Random Forest and Adaboost Tree-Based Ensemble Classification and Spectral Band Selection

Random forest and Adaboost are two tree-based ensemble classifiers. These classifiers serve two purposes:

1. Help select hyperspectral bands that are important as well as those that are redundant.
2. Classify hyperspectral data through decision tree-based classifiers.

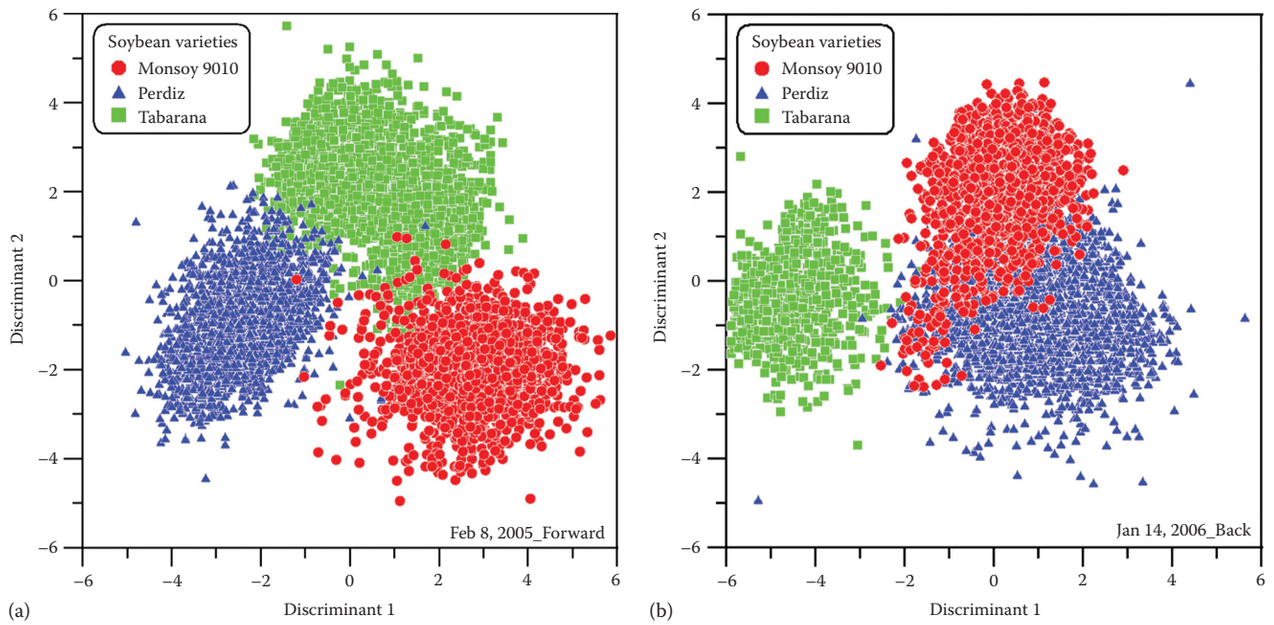


**FIGURE 9.18** Species soybeans. View angle effects on the discrimination of soybean varieties and on the relationships between vegetation indices and yield using off-nadir Hyperion data. Projection of the Hyperion discriminant scores of the three soybean varieties in the (a) forward and (b) backscattering directions for different years. (From Galvao, L.S. et al., Crop type discrimination using hyperspectral data, Chapter 17, in Thenkabail, P.S., Lyon, G.J., and Huete, A., *Hyperspectral Remote Sensing of Vegetation*, CRC Press/Taylor & Francis Group, Boca Raton, FL/London, U.K./New York, 2009, pp. 397–422.)

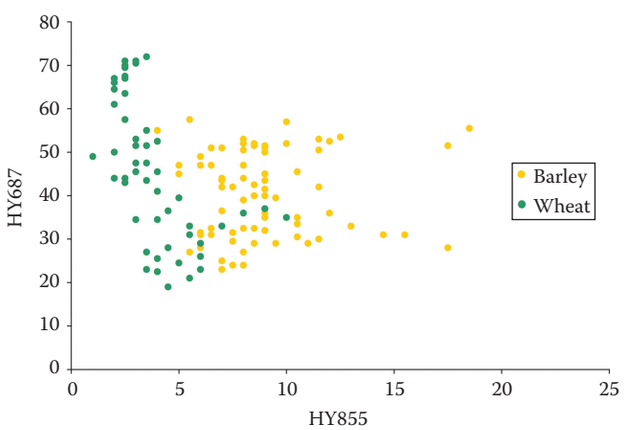


**FIGURE 9.19** Differentiating corn from soybeans using two hyperspectral narrowbands.

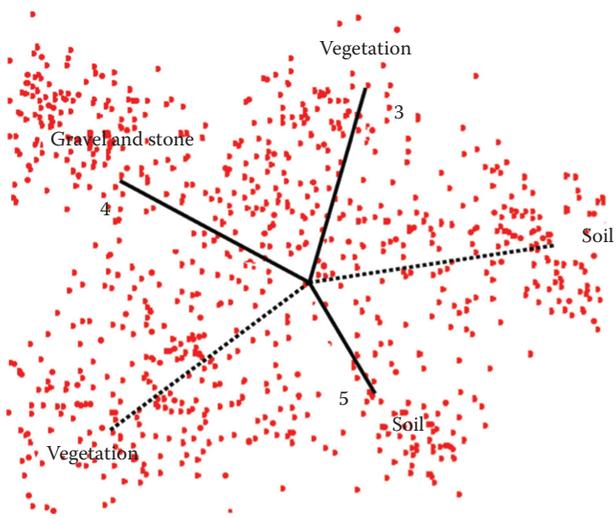


**FIGURE 9.20** End member. Arid land characterization with EO-1 Hyperion hyperspectral data. End member extraction in n-dimension visualizer using bands 3, 4, and 5 of the minimum noise fraction (MNF) transform Hyperion image. (From Jafari, R. and Lewis, M.M., *Int. J. Appl. Earth Obs. Geoinf.*, 19, 298, 2012.)

This approach has been discussed in great detail by Chan and Paelinckx (2008) for thorough classification of detailed ecotopes using hyperspectral data (Figures 9.25 and 9.26). They gathered extensive hyperspectral data for (Figure 9.25) (1) 6 grassland classes and (2) 10 tree classes. In terms of accuracy performance, random forest and Adaboost are almost the same, and both have outperformed a neural network classifier (Chan and Paelinckx, 2008). Both feature selection routines, the best-first search and the out-of-bag ranking index under random forest, are successful in identifying substantially smaller band subsets that attained almost the same accuracy as all the bands (e.g., Figure 9.24; Chan and Paelinckx, 2008). There are many approaches to selecting the spectral wavebands for obtaining best classification results. For agriculture

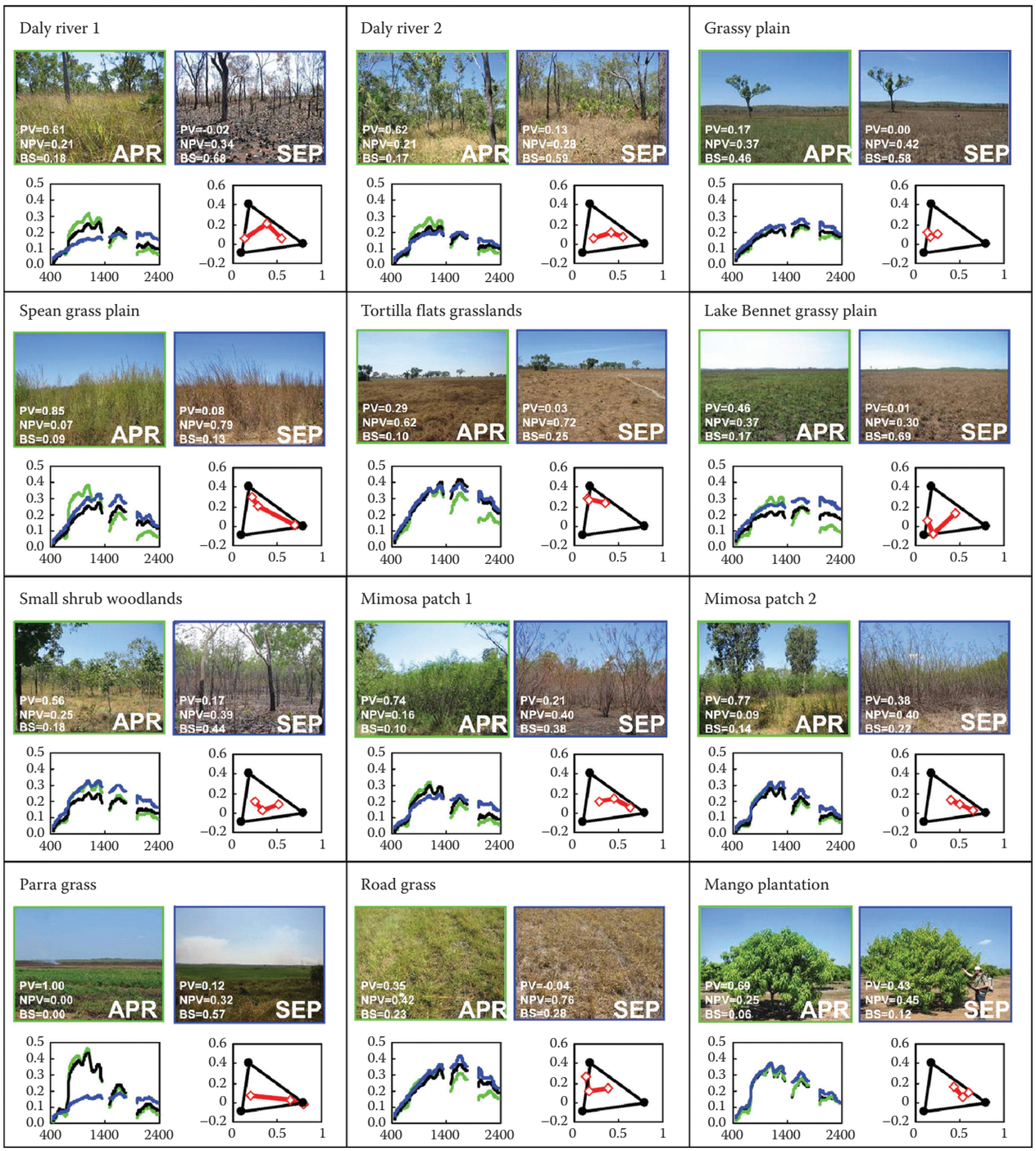


**FIGURE 9.21** Unmixing qualitative assessment of Hyperion unmixing of vegetation fractional cover. Qualitative validation of the fractional cover estimated with Hyperion imagery. Each set of pictures and graphs corresponds to one of 12 sites visited from May 16 to 19 and August 29 to 31, 2005. The left graphs show the reflectance spectra derived from Hyperion images for the April (green curve), July (black curve), and September (blue curve) images from 400 to 2400 nm. The right graphs show the position of each spectrum in the normalized difference vegetation index or NDVI (x-axis) (detecting live, green vegetation) and cellulose absorption index or CAI (y-axis) (detecting non-photosynthetic vegetation) space from April to September (red dots and line) and the position of the end members (black lines). The derived photosynthetic vegetation ($f_{PV}$), non-photosynthetic vegetation ($f_{NPV}$), and bare soil ($f_{BS}$) are shown in each picture and are critical for natural resource management and for modeling carbon dynamics. (From Guerschman, J.P. et al., *Remote Sens. Environ.*, 113, 928, 2009.)

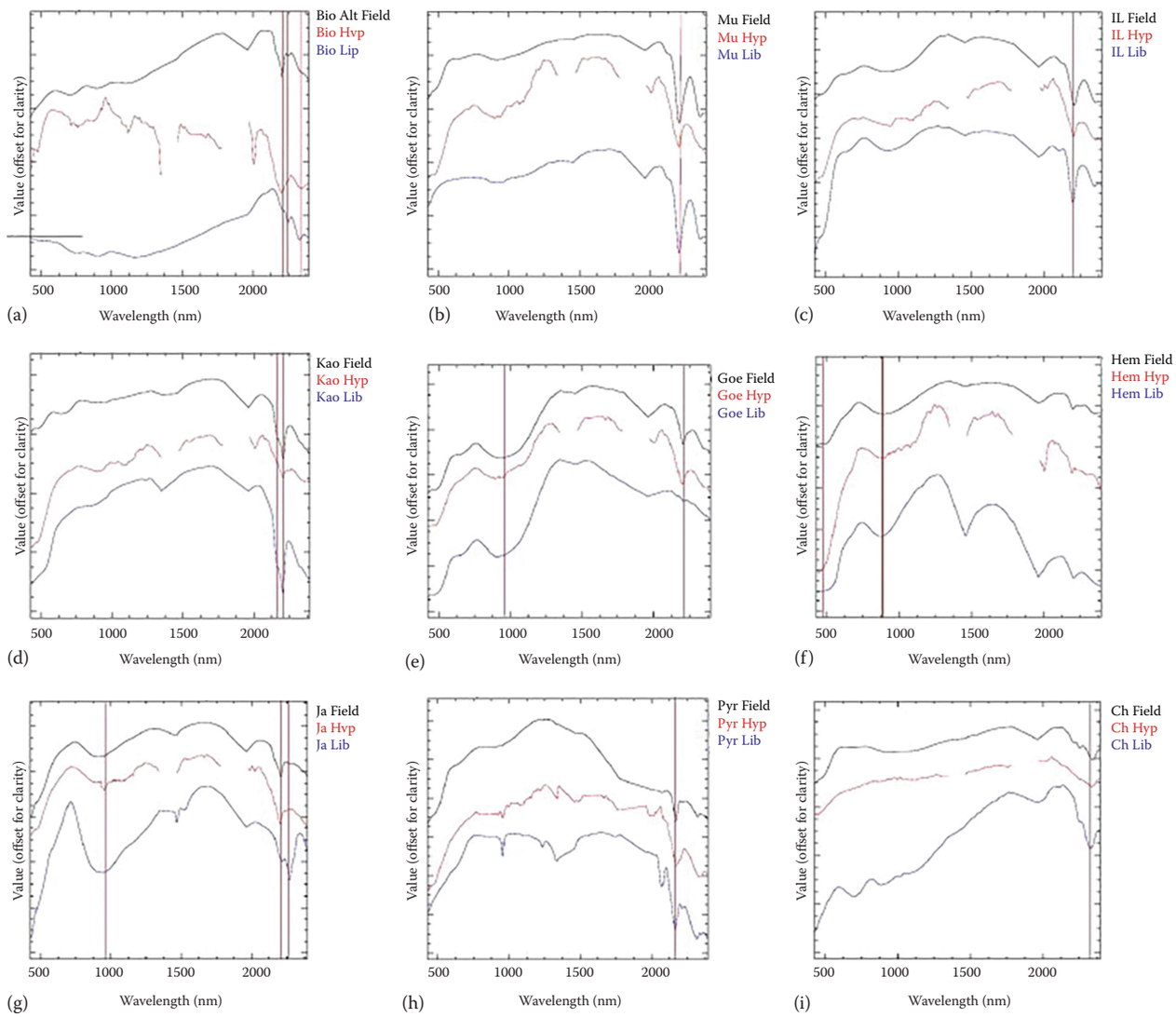


**FIGURE 9.22** Mineral mapping. Subpixel mineral mapping of a porphyry copper belt using EO-1 Hyperion data. Mineral spectra extracted from Hyperion comparing to convolved spectra from field samples and reference library spectra. (a) Biotite (Bio), (b) Muscovite (Mu), (c) Illite (Il), (d) Kaolinite (Kao), (e) Goethite (Goe), (f) Hem (Hem), (g) Jarosite (Ja), (h) pyrophyllite (Pyr), and (i) Chlorite (Ch). Hyp and Lib are abbreviations of Hyperion and Library, respectively. The red vertical lines indicate locations of diagnostic absorption features. (From Hosseinjani Zadeh, M. et al., *Adv. Space Res.*, 53, 440, 2014.)

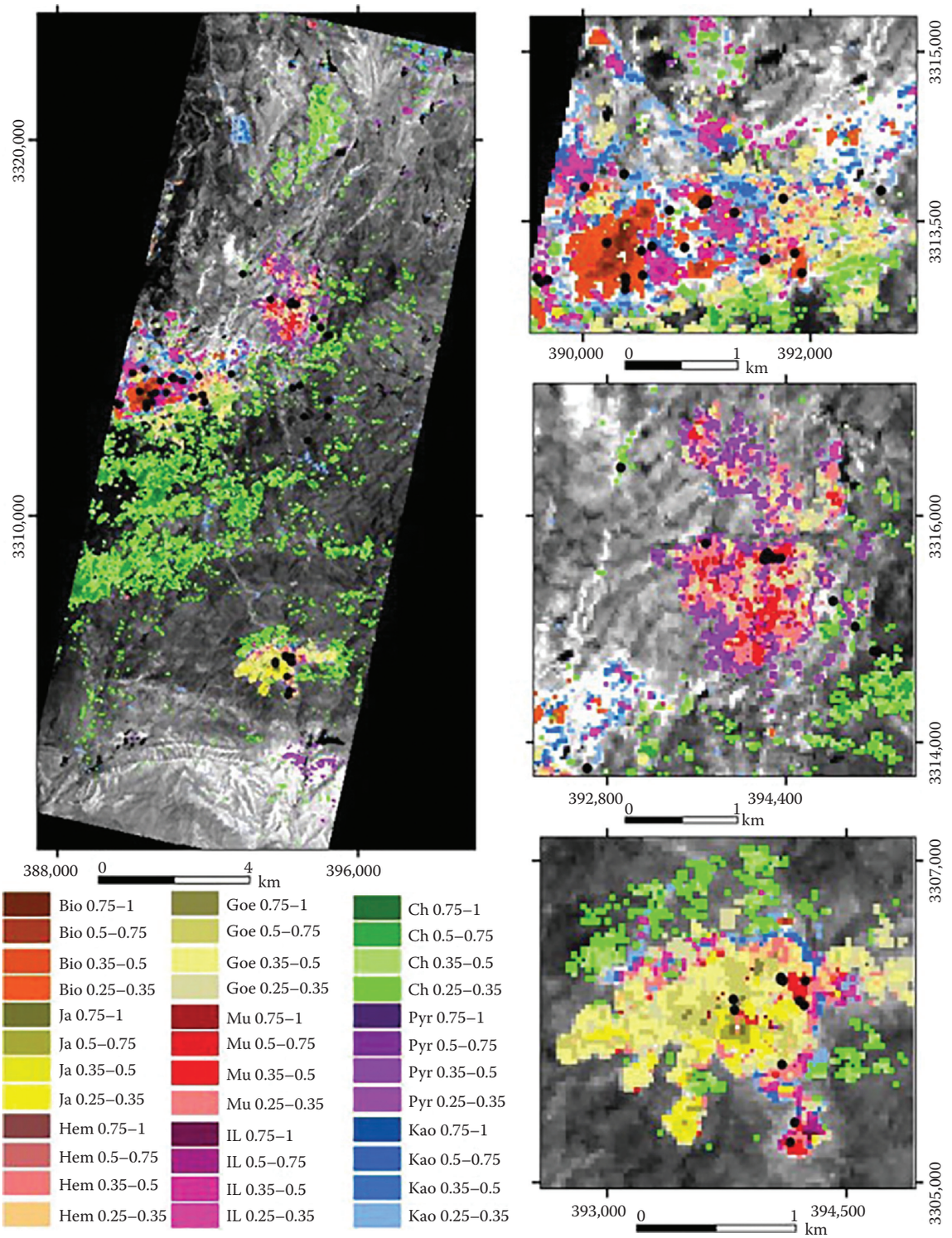


**FIGURE 9.23** Mineral mapping. Subpixel mineral mapping of a porphyry copper belt using EO-1 Hyperion data. Thematic mineral maps using subpixel mixture tuned matched filtering (MTMF) method. (a) Final classification image map of alteration minerals derived from MTMF algorithm. (b) Sarcheshmeh mine, (c) Sereidun, and (d) Darrehzar. Bio, Mu, Il, Kao, Goe, Hem, Ja, Pyr, and Ch indicate Biotite, Muscovite, Illite, Kaolinite, Goethite, Hematite, Jarosite, pyrophyllite, and Chlorite, respectively. These values indicate percentages of each mineral at the pixel. For instance, value of 0.25 shows that 25% of pixel contains the selected mineral. (From Hosseinjani Zadeh, M. et al., *Adv. Space Res.*, 53, 440, 2014.)

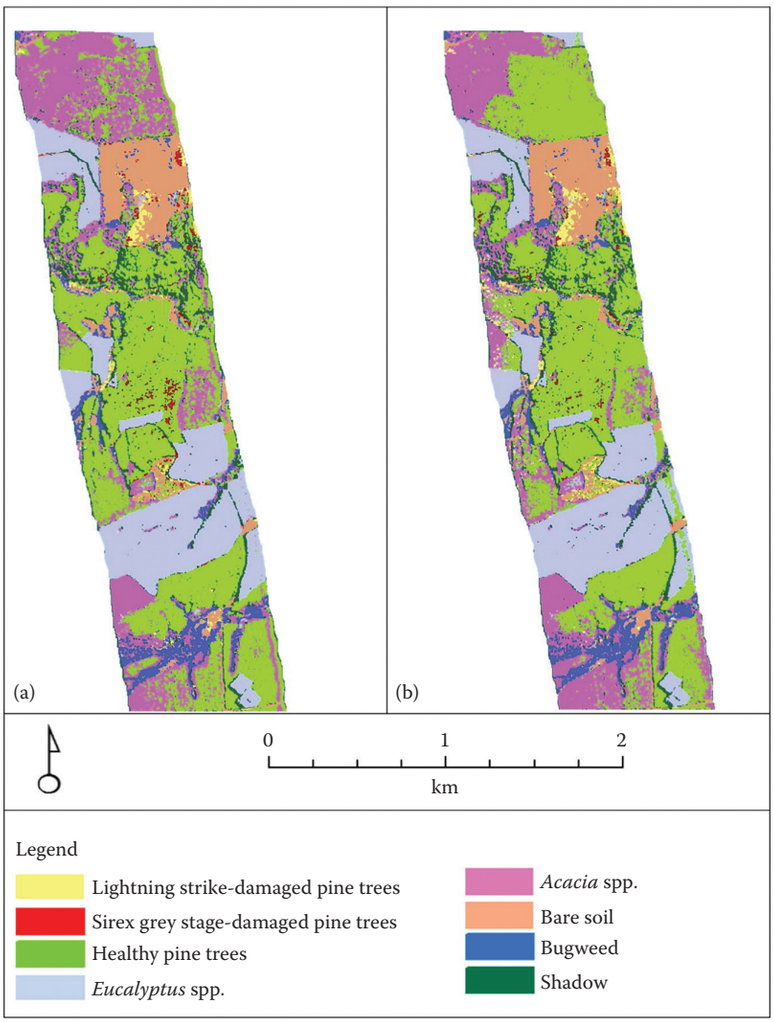


**FIGURE 9.24** SVM. Detecting Sirex noctilio gray-attacked and lightning-struck pine trees using airborne hyperspectral data, random forest, and support vector machine classifiers. Classification maps obtained using support vector machine (SVM) classification algorithm, all (a) and the 51 most important (b) Airborne Imaging System for different Applications (AISA) Eagle spectral bands. The AISA image spatial resolution was about 2 m, and there were 272 spectral bands ranging from 393.23 to 994.09 nm (VNIR: visible near-infrared) with bandwidths between 2 and 4 nm. (From Abdel-Rahman, E.M. et al., *ISPRS J. Photogramm. Remote Sens.*, 88, 48, 2014.)

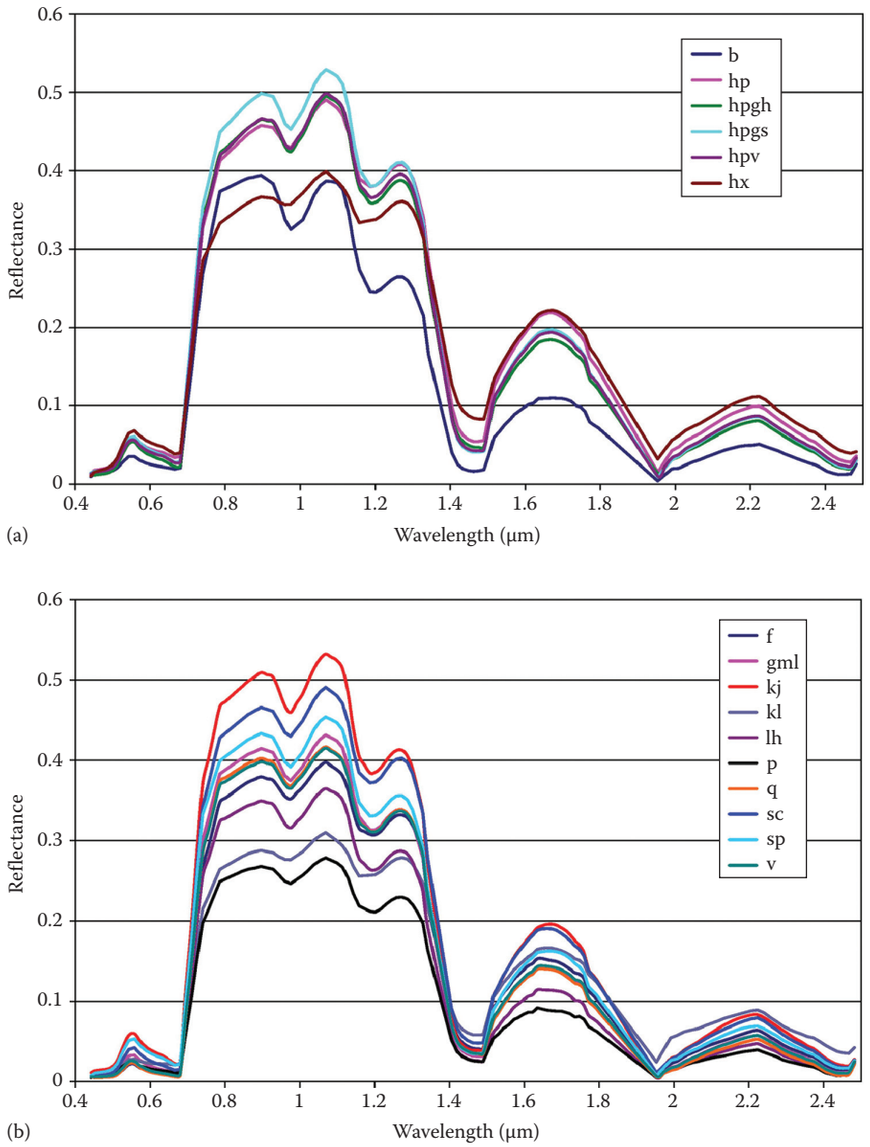


**FIGURE 9.25** Evaluation of Random Forest and Adaboost tree-based ensemble classification and spectral band selection for ecotope mapping using airborne hyperspectral imagery. Mean spectrum of the (a) 6 grassland classes and (b) 10 tree classes. *Notes*: b, grassland, arable land; hp, grassland, species poor improved grassland (normally more homogenous for the whole parcel); hpgh, grassland, semi-natural grassland; hpgs, grassland, species rich improved grassland (between hpgh and hp); hpv, grassland, grassland with patches hp and either patches hpgs or hpgh; hx, grassland, grass monocultures (equal to arable land sown with grasses of one or more years); f, tree/tall_veg, deciduous forest<comma> dominated by beech (*Fagus* sp.); gml, tree/tall_veg, plantation of deciduous tree species other than beech, oak, alder, and poplar; kj, tree/tall_veg, tall tree orchard; kl, tree/tall_veg, low tree orchard; lh, tree/tall_veg, poplar plantation; p, tree/tall_veg, conifer plantation; q, tree/tall_veg, deciduous forest<comma> dominated by oak trees (*Quercus* sp.); sp, tree/tall_veg sc, scrubs of clearings and scrubs on abandoned land; sp, tree/tall_veg, thorn ticket; v, tree/tall_veg,Woodland of alluvial soil<comma> fens and bogs (mostly dominated by alder, *Alnus* sp.). (From Chan, J.C.-W. and Paelinckx, D., *Remote Sens. Environ.*, 112, 2999, 2008.)

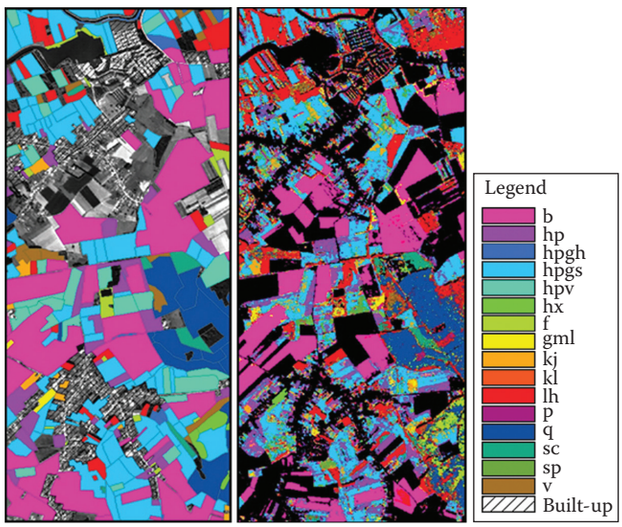


**FIGURE 9.26** Evaluation of random forest and Adaboost tree-based ensemble classification and spectral band selection for ecotope mapping using airborne hyperspectral imagery. On the left is the ground truth image of the biological valuation map. On the right is the biological valuation map classification based on airborne hyperspectral data using 99 trials of Adaboost with 21 bands selected by the best-first search method. The black areas represent unclassified land covers that have been masked out. (From Chan, J.C.-W. and Paelinckx, D., *Remote Sens. Environ.*, 112, 2999, 2008.)

**TABLE 9.5** Best Hyperspectral Narrowband (HNB) Combinations Based on Number of Bands Available to Classify Crops or Vegetation

| | |
|---|---|
| Best 4 bands | 550, 680, 850, 970 |
| Best 6 bands | 550, 680, 850, 970, 1075, 1450 |
| Best 8 bands | 550, 680, 850, 970, 1075, 1180, 1450, 2205 |
| Best 10 bands | 550, 680, 720, 850, 970, 1075, 1180, 1245, 1450, 2205 |
| Best 12 bands | 550, 680, 720, 850, 910, 970, 1075, 1180, 1245, 1450, 1650, 2205 |
| Best 16 bands | 490, 515, 550, 570, 680, 720, 850, 900, 970, 1075, 1180, 1245, 1450, 1650, 1950, 2205 |
| Best 20 bands | 490, 515, 531, 550, 570, 680, 720, 850, 900, 970, 1075, 1180, 1245, 1450, 1650, 1725, 1950, 2205, 2262, 2359 |

*Sources:* Adapted and modified from Thenkabail, P.S. et al., 2012, 2013; Thenkabail, P.S. et al., *Photogramm. Eng. Remote Sens.*, 80, 697, 2014.

and vegetation studies, one could use various combination of band selection (e.g., Table 9.5) depending on the number of bands one decided to use, classification accuracies desired, and the need to overcome Hughes's phenomenon.

## 9.14 Conclusions

This chapter provides an overview of hyperspectral remote sensing for terrestrial applications. First, the chapter defines hyperspectral remote sensing or imaging spectroscopy. Second, characteristics of hyperspectral data acquired from three distinct platforms are discussed: (1) ground-based or handheld or truck-mounted spectroradiometers, (2) airborne, and (3) spaceborne. Third, the needs for data mining to eliminate redundant bands are discussed. Various data mining methods are presented. Fourth, the importance of understanding Hughes's phenomenon and approaches to overcome the same are highlighted. Fifth, methods of hyperspectral analysis are presented and discussed. These methods include feature extraction methods and information extraction methods. OHNBs best suited for agricultural and vegetation studies are determined from meta-analysis. HVIs, two-band and multi-band versions, best suited for agricultural and vegetation studies are also determined from meta-analysis. The WSA was performed through SMTs and continuum removal derivative HVIs. Hyperspectral image classification for land cover and species types was performed using such methods like SMA, SVMs, and tree-based ensemble classifiers such as random forest and Adaboost.

## References

Abdel-Rahman, E.M., Mutanga, O., Adam, E., Ismail, R., 2014. Detecting Sirex noctilio grey-attacked and lightning-struck pine trees using airborne hyperspectral data, random forest and support vector machines classifiers. *ISPRS Journal of Photogrammetry and Remote Sensing*, 88, 48–59.

Alchanatis, V., Cohen, Y., 2012. Spectral and spatial methods for hyperspectral image analysis for estimation of biophysical and biochemical properties of agricultural crops. Chapter 13, in Thenkabail, P.S., Lyon, G.J., and Huete, A. *Hyperspectral Remote Sensing of Vegetation*. CRC Press/Taylor & Francis Group, Boca Raton, FL/London, U.K./New York. pp. 239–308.

Andrew, M.E., Ustin, S.L., 2008. The role of environmental context in mapping invasive plants with hyperspectral image data. *Remote Sensing of Environment*, 112, 4301–4317.

Bajwa, S., Kulkarni, S.S., 2012. Hyperspectral data mining. Chapter 4, in Thenkabail, P.S., Lyon, G.J., and Huete, A. *Hyperspectral Remote Sensing of Vegetation*. CRC Press/Taylor & Francis Group, Boca Raton, FL/London, U.K./New York. pp. 93–120.

Ben-Dor, E., 2012. Characterization soil properties using reflectance spectroscopy. Chapter 22, in Thenkabail, P.S., Lyon, G.J., and Huete, A. *Hyperspectral Remote Sensing of Vegetation*. CRC Press/Taylor & Francis Group, Boca Raton, FL/London, U.K./New York. pp. 513–560.

Boardman, J. W., Kruse, F. A., 1994. Automated spectral analysis: A geological example using AVIRIS data, north Grapevine Mountains, Nevada. In *Proceedings of ERIM 10th Thematic Conference on Geologic Remote Sensing*, Environmental Research Institute of Michigan, Ann Arbor, MI. pp. I-407–I-418.

Chan, J.C.-W., Paelinckx, D., 2008. Evaluation of Random Forest and Adaboost tree-based ensemble classification and spectral band selection for ecotope mapping using airborne hyperspectral imagery. *Remote Sensing of Environment*, 112, 2999–3011.

Chander, G., Markham, B.L., Helder, D.L. 2009. Summary of current radiometric calibration coefficients for Landsat MSS, TM, ETM+, and EO-1 ALI sensors. *Remote Sensing of Environment*, 113, 893–903.

Chavez, P.S., 1988. An improved dark-object subtraction technique for atmospheric scattering correction of multispectral data. *Remote Sensing of Environment*, 24, 459–479.

Chavez, P.S., 1989. Radiometric calibration of Landsat thematic mapper multispectral images. *Photogrammetric Engineering and Remote Sensing*, 55, 1285–1294.

Clark, M.L., 2012. Identification of canopy species in tropical forests using hyperspectral data. Detecting and mapping invasive species using hyperspectral data. Chapter 18, in Thenkabail, P.S., Lyon, G.J., and Huete, A. *Hyperspectral Remote Sensing of Vegetation*. CRC Press/Taylor & Francis Group, Boca Raton, FL/London, U.K./New York. pp. 423–446.

Colombo, R., Lorenzo, B., Michele, M., Micol, R., Cinzia, P., 2012. Optical remote sensing of vegetation water content. Chapter 10, in Thenkabail, P.S., Lyon, G.J., and Huete, A. *Hyperspectral Remote Sensing of Vegetation*. CRC Press/Taylor & Francis Group, Boca Raton, FL/London, U.K./New York. p. 227.

Colomina, I., Molina, P. 2014. Unmanned aerial systems for photogrammetry and remote sensing: A review. *ISPRS Journal of Photogrammetry and Remote Sensing*, 92, 79–97, ISSN 0924–2716, http://dx.doi.org/10.1016/j.isprsjprs.2014.02.013.

Elvidge, C.D., Yuan, D., Weerackoon, R.D., Lunetta, R.S. 1995. Relative radiometric normalization of landsat multispectral scanner (MSS) data using an automatic scattergram controlled regression. *Photogrammetric Engineering and Remote Sensing*, 61, 1255–1260.

Fayyad, U., Piatetsky-Shapiro, G., Smyth, P., 1996. The KDD process for extracting useful knowledge from volumes of data. *Communications of the ACM*, 39, 27–34.

Galvão, L.S., 2012. Crop type discrimination using hyperspectral data. Chapter 17, in Thenkabail, P.S., Lyon, G.J., and Huete, A. *Hyperspectral Remote Sensing of Vegetation*. CRC Press/Taylor & Francis Group, Boca Raton, FL/London, U.K./New York. pp. 397–422.

Galvão, L.S., Roberts, D.A., Formaggio, A.R., Numata, I., and Breunig, F.M., 2009. View angle effects on the discrimination of soybean varieties and on the relationships between vegetation indices and yield using off-nadir Hyperion data. *Remote Sensing of Environment* 113, 846–856, DOI:10.1016/j.rse.2008.12.010.

Gitelson, A., 2012a. Non-destructive estimation of foliar pigment (chlorophylls, carotenoids, and anthocyanins) contents: Evaluating a semi-analytical three-band model. Chapter 6, in Thenkabail, P.S., Lyon, G.J., and Huete, A. *Hyperspectral Remote Sensing of Vegetation*. CRC Press/Taylor & Francis Group/Boca Raton, FL/London, U.K./New York. pp. 141–166.

Gitelson, A., 2012b. Remote estimation of crop biophysical characteristics at various scales. Chapter 15, in Thenkabail, P.S., Lyon, G.J., and Huete, A. *Hyperspectral Remote Sensing of Vegetation*. CRC Press/Taylor & Francis Group, Boca Raton, FL/London, U.K./New York. pp. 329–360.

Gnyp, M.L., Bareth, G., Li, F., Lenz-Wiedemann, V.I., Koppe, W., Miao, Y., Hennig, S.D., Jia, L., Laudien, R., Chen, X., 2014. Development and implementation of a multiscale biomass model using hyperspectral vegetation indices for winter wheat in the North China Plain. *International Journal of Applied Earth Observation and Geoinformation*, 33, 232–242.

Goetz, A.F.H., 1992. Imaging Spectrometry for Earth Observations. *Episodes*, 15, 7–14.

Green, A. A., Berman, M., Switzer, P., Craig, M.D., 1988. A transformation for ordering multispectral data in terms of image quality with implications for noise removal. *IEEE Transactions on Geosciences and Remote Sensing*, 26(1), 65–74.

Guerschman, J.P., Hill, M.J., Renzullo, L.J., Barrett, D.J., Marks, A.S., Botha, E.J., 2009. Estimating fractional cover of photosynthetic vegetation, non-photosynthetic vegetation and bare soil in the Australian tropical savanna region upscaling the EO-1 Hyperion and MODIS sensors. *Remote Sensing of Environment*, 113, 928–945.

Guo, X., Huang, X., Zhang, L., Zhang, L., 2013. Hyperspectral image noise reduction based on rank-1 tensor decomposition. *ISPRS Journal of Photogrammetry and Remote Sensing*, 83, 50–63.

Hernández-Clemente, R., Navarro-Cerrillo, R.M., Suárez, L., Morales, F., Zarco-Tejada, P.J., 2011. Assessing structural effects on PRI for stress detection in conifer forests. *Remote Sensing of Environment*, 115, 2360–2375.

Hosseinjani Zadeh, M., Tangestani, M.H., Roldan, F.V., Yusta, I., 2014. Sub-pixel mineral mapping of a porphyry copper belt using EO-1 Hyperion data. *Advances in Space Research*, 53, 440–451.

Jafari, R., Lewis, M.M., 2012. Arid land characterisation with EO-1 Hyperion hyperspectral data. *International Journal of Applied Earth Observation and Geoinformation*, 19, 298–307.

Jensen, J.R. 2004. *Introductory Digital Image Processing: A Remote Sensing Perspective* (3rd edn.). Prentice-Hall, Upper Saddle River, New Jersey.

Lausch, A., Schmidt, A., Tischendorf, L., 2014. Data mining and linked open data–New perspectives for data analysis in environmental research. *Ecological Modelling,* 295, 5–17.

Li, J., Li, C., Xhao, D., Gang, C., 2012. Hyperspectral narrowbands and their indices on assessing nitrogen contents of cotton crop applications. Chapter 24, in Thenkabail, P.S., Lyon, G.J., and Huete, A. *Hyperspectral Remote Sensing of Vegetation*. CRC Press/Taylor & Francis Group, Boca Raton, FL/London, U.K./New York. pp. 579–590.

Mariotto, I., Thenkabail, P.S., Huete, A., Slonecker, E.T., Platonov, A., 2013. Hyperspectral versus multispectral crop-productivity modeling and type discrimination for the HyspIRI mission. *Remote Sensing of Environment*, 139, 291–305.

Markham, B.L. and Barker, J.L., 1987. Radiometric properties of U.S. processed Landsat MSS data. *Remote Sensing of Environment*, 22, 39–71.

Marshall, M., Thenkabail, P., 2014. Biomass modeling of four leading world crops using hyperspectral narrowbands in support of HyspIRI mission. *Photogrammetric Engineering and Remote Sensing*, 80, 757–772.

Middleton, E., Huemmrich, K.F., Cheng, Y., B, Margolis, H., 2012. Spectral bio-indicators of photosynthetic efficiency and vegetation stress. Chapter 12, in Thenkabail, P.S., Lyon, G.J., and Huete, A. *Hyperspectral Remote Sensing of Vegetation*. CRC Press/Taylor & Francis Group, Boca Raton, FL/London, U.K./New York. pp. 265–288.

Miura, T., Yoshioka, H., 2012. Hyperspectral data in long-term cross-sensor vegetation index continuity for global change studies. Chapter 26, in Thenkabail, P.S., Lyon, G.J., and Huete, A. 2011. *Hyperspectral Remote Sensing of Vegetation*. CRC Press/Taylor & Francis Group, Boca Raton, FL/London, U.K./New York. pp. 611–636.

Neckel, H. and Labs, D., 1984. The solar radiation between 3300 and 12500 A. *Solar Physics* 90, 205–258. DOI: 10.1007/BF00173953.

Numata, I., 2012. Characterization on pastures using field and imaging spectrometers. Chapter 9, in Thenkabail, P.S., Lyon, G.J., and Huete, A. 2012. *Hyperspectral Remote Sensing of Vegetation*. CRC Press/Taylor & Francis Group, Boca Raton, FL/London, U.K./New York. pp. 207–226.

Ortenberg, F., 2012. Hyperspectral sensor characteristics airborne, spaceborne, hand-held, and truck-mounted and integration of hyperspectral data with LiDAR. Chapter 2, in Thenkabail, P.S., Lyon, G.J., and Huete, A. 2012. *Hyperspectral Remote Sensing of Vegetation*. CRC Press/Taylor & Francis Group, Boca Raton, FL/London, U.K./New York. pp. 39–68.

Plaza, A., Plaza, J., Martin, G., S, S., 2012. Hyperspectral data processing algorithms. Chapter 5, in Thenkabail, P.S., Lyon, G.J., and Huete, A. 2012. *Hyperspectral Remote Sensing of Vegetation*. CRC Press/Taylor & Francis Group, Boca Raton, FL/London, U.K./New York. pp. 121–140.

Pu, R., 2012. Detecting and mapping invasive plant species by using hyperspectral data. Chapter 19, in Thenkabail, P.S., Lyon, G.J., and Huete, A. 2012. *Hyperspectral Remote Sensing of Vegetation*. CRC Press/Taylor & Francis Group, Boca Raton, FL/London, U.K./New York. pp. 447–468.

Qi, J., Inoue, Y., Wiangwang, N., 2012. Hyperspectral sensor systems and data characteristics in global change studies. Chapter 3, in Thenkabail, P.S., Lyon, G.J., and Huete, A. 2012. *Hyperspectral Remote Sensing of Vegetation*. CRC Press/Taylor & Francis Group, Boca Raton, FL, London, FL, New York. pp. 69–92.

Ramsey III, E.W., Rangoonwala, A., 2012. Hyperspectral remote sensing of wetlands. Chapter 21, in Thenkabail, P.S., Lyon, G.J., and Huete, A. 2012. *Hyperspectral Remote Sensing of Vegetation*. CRC Press/Taylor & Francis Group, Boca Raton, FL/London, U.K./New York. pp. 487–512.

Roberts, D.A., 2012.. Hyperspectral vegetation indices. Chapter 14, in Thenkabail, P.S., Lyon, G.J., and Huete, A. 2012. *Hyperspectral Remote Sensing of Vegetation*. CRC Press/Taylor & Francis Group, Boca Raton, FL, London, U.K./New York. pp. 309–328.

SAS, 2009. SAS Institute. SAS/STAT user's guide and software release, version 9.2 Ed. SAS Institute, Cary, NC.

Slonecker, T., 2012. Hyperspectral analysis of the effects of heavy metals on vegetation reflectance. Chapter 23, in Thenkabail, P.S., Lyon, G.J., and Huete, A. 2012. *Hyperspectral Remote Sensing of Vegetation*. CRC Press/Taylor & Francis Group, Boca Raton, FL/London, U.K./New York. pp. 561–578.

Stroppiana, D., Fava, F., Boschetti, M., Brivio, P.A., 2012. Estimation of nitrogen content in crops and pastures using hyperspectral vegetation indices. Chapter 11, in Thenkabail, P.S., Lyon, G.J., and Huete, A. 2012. *Hyperspectral Remote Sensing of Vegetation*. CRC Press/Taylor & Francis Group, Boca Raton, FL/London, U.K./New York. pp. 245–264.

Tanner, R., 2013. Data mining–das etwas andere eldorado. *Technologie IT-Methoden*, 8, 37–42.

Thenkabail, P., GangadharaRao, P., Biggs, T., Krishna, M., Turral, H., 2007. Spectral matching techniques to determine historical land-use/land-cover (LULC) and irrigated areas using time-series 0.1-degree AVHRR Pathfinder datasets. *Photogrammetric Engineering and Remote Sensing* 73, 1029–1040.

Thenkabail, P.S., Enclona, E.A., Ashton, M.S., Legg, C., De Dieu, M.J., 2004a. Hyperion, IKONOS, ALI, and ETM+ sensors in the study of African rainforests. *Remote Sensing of Environment* 90, 23–43.

Thenkabail, P.S., Enclona, E.A., Ashton, M.S., Van Der Meer, B., 2004b. Accuracy assessments of hyperspectral waveband performance for vegetation analysis applications. *Remote Sensing of Environment* 91, 354–376.

Thenkabail, P.S., Gumma, M.K., Teluguntla, P., Mohammed, I.A., 2014. Hyperspectral remote sensing of vegetation and agricultural crops. *Photogrammetric Engineering and Remote Sensing*, 80, 697–709.

Thenkabail, P.S., Hanjra, M.A., Dheeravath, V., Gumma, M., 2010. A holistic view of global croplands and their water use for ensuring global food security in the 21st century through advanced remote sensing and non-remote sensing approaches. *Remote Sensing*, 2, 211–261.

Thenkabail, P.S., Lyon, G.J., Huete, A., 2012a. Advances in hyperspectral remote sensing of vegetation and agricultural crops. Chapter 1, in Thenkabail, P.S., Lyon, G.J., and Huete, A. 2012. *Hyperspectral Remote Sensing of Vegetation*. CRC Press/Taylor & Francis Group, Boca Raton, FL/London, U.K./New York. pp. 3–29.

Thenkabail, P.S., Lyon, J.G., Huete, A., 2012b. Synthesis on hyperspectral remote sensing of vegetation. Chapter 28, in Thenkabail, P.S., Lyon, G.J., and Huete, A. 2012. *Hyperspectral Remote Sensing of Vegetation: Current Status and Future Possibilities*. CRC Press/Taylor & Francis Group, Boca Raton, FL/London, U.K./New York. pp. 663–668.

Thenkabail, P.S., Mariotto, I., Gumma, M.K., Middleton, E.M., Landis, D.R., and Huemmrich, F.K., 2013. Selection of hyperspectral narrowbands (HNBs) and composition of hyperspectral twoband vegetation indices (HVIs) for biophysical characterization and discrimination of crop types using field reflectance and Hyperion/EO-1 data. *IEEE Journal of Selected Topics in Applied Earth Observations And Remote Sensing*, 6(2), 427–439, APRIL 2013. Doi:HYPERLINK "http://dx.doi.org/10.1109/JSTARS.2013.2252601" \t "blank" 10.1109/JSTARS.2013.2252601.

Thenkabail, P.S., Smith, R.B., and De-Pauw, E. 2002. Evaluation of narrowband and broadband vegetation indices for determining optimal hyperspectral wavebands for agricultural crop characterization. *Photogrammetric Engineering and Remote Sensing*. 68(6), 607–621.

Thenkabail, P.S., Smith, R.B., De Pauw, E., 2000. Hyperspectral vegetation indices and their relationships with agricultural crop characteristics. *Remote Sensing of Environment*, 71, 158–182.

Thenkabail, P.S., Wu, Z., 2012. An automated cropland classification algorithm (ACCA) for Tajikistan by combining Landsat, MODIS, and secondary data. *Remote Sensing*, 4, 2890–2918.

Thomas, V., 2012. Hyperspectral remote sensing for forest management. Chapter 20, in Thenkabail, P.S., Lyon, G.J., and Huete, A. 2012. *Hyperspectral Remote Sensing of Vegetation*. CRC Press/Taylor & Francis Group, Boca Raton, FL/London, U.K./New York. pp. 469–486.

Tits, L., De Keersmaecker, W., Somers, B., Asner, G.P., Farifteh, J., Coppin, P., 2012. Hyperspectral shape-based unmixing to improve intra-and interclass variability for forest and agro-ecosystem monitoring. *ISPRS Journal of Photogrammetry and Remote Sensing*, 74, 163–174.

Torres-Sánchez, J., Peña, J. M., de Castro, A.I., López-Granados, F. 2014. Multi-temporal mapping of the vegetation fraction in early-season wheat fields using images from UAV. *Computers and Electronics in Agriculture*, 103, 104–113, ISSN 0168–1699, http://dx.doi.org/10.1016/j. compag.2014.02.009. (http://www.sciencedirect.com/science/article/pii/S0168169914000568).

Vaughan, R.G., Titus, T.N., Johnson, J.R., Hagerty, J., Gaddis, L., Soderblom, L.A., Geissler, P., 2011. Hyperspectral analysis of rocky surfaces on the earth and other planetary systems. Chapter 27, in Thenkabail, P.S., Lyon, G.J., and Huete, A. 2012. *Hyperspectral Remote Sensing of Vegetation*. CRC Press/Taylor & Francis Group, Boca Raton, FL/London, U.K./New York. pp. 637–662.

Vermote, E.F., El Saleous, N.Z., Justice, C.O., 2002. Atmospheric correction of MODIS data in the visible to middle infrared: First results. *Remote Sensing of Environment*, 83(1–2), 97–111.

Yao, H., Tang, L., Tian, L., Brown, R.L., Bhatnagar, D., Cleveland, T.E., 2011. Using hyperspectral data in precision farming applications. Chapter 25, in Thenkabail, P.S., Lyon, G.J., and Huete, A. 2012. *Hyperspectral Remote Sensing of Vegetation*. CRC Press/Taylor & Francis Group, Boca Raton, FL/London, U.K./New York. pp. 591–610.

Zhang, Y., 2012. Forest leaf chlorophyll content study using hyperspectral remote sensing. Chapter 7, in Thenkabail, P.S., Lyon, G.J., and Huete, A. 2012. *Hyperspectral Remote Sensing of Vegetation*. CRC Press/Taylor & Francis Group, Boca Raton, FL/London, U.K./New York. pp. 167–186.

Zhu, Y., Wang, W., Yao, X., 2012. Estimating leaf nitrogen concentration (LNC) of cereal crop with hyperspectral data. Chapter 8, in Thenkabail, P.S., Lyon, G.J., and Huete, A. 2012. *Hyperspectral Remote Sensing of Vegetation*. CRC Press/Taylor & Francis Group, Boca Raton, FL/London, U.K./New York. pp. 187–206.